J Nonlinear Math Phys
https://doi.org/10.1007/s44198-026-00448-z

Article in Press

# Adaptive Shooting Analysis of Magnetized Micropolar Flow in Transpiration-Controlled Riga Channels with Radiative and Cross-Diffusion Effects

Received: 5 January 2026
Accepted: 15 June 2026
Published online: 05 July 2026

Cite this article as: Ahmed S.E., Arafa A.A.M., Hussein S.A. *et al.* Adaptive Shooting Analysis of Magnetized Micropolar Flow in Transpiration-Controlled Riga Channels with Radiative and Cross-Diffusion Effects. *J Nonlinear Math Phys* (2026). https://doi.org/10.1007/s44198-026-00448-z

Sameh E. Ahmed, Anas A. M. Arafa, Sameh A. Hussein & M. Khalil

# Adaptive Shooting Analysis of Magnetized Micropolar Flow in Transpiration-Controlled Riga Channels with Radiative and Cross-Diffusion Effects

*Sameh E. Ahmed[1], Anas A. M. Arafa[2], Sameh A. Hussein[3,4], M. Khalil[5]*

[1]*Department of Mathematics, Faculty of Science, King Khalid University, Abha, Saudi Arabia*

[2]*Department of Mathematics, College of Science, Qassim University, Buraydah, Saudi Arabia.*

[3]*Department of Mathematics, Faculty of Science, Zagazig University, Zagazig, Egypt*

[4]*Mathematics Education Program, Faculty of Education and arts, Sohar University, P.O. Box 44, Sohar 311, Oman.*

[5]*Department of Mathematics, Faculty of Engineering, October University for Modern Sciences and Arts (MSA), Giza, Egypt*

*E-mails: sehassan@kku.edu.sa, a.arafa@qu.edu.sa, sameh.moawad@zu.edu.eg, mkibrahim@msa.edu.eg*

*Corresponding author: Sameh E. Ahmed*

**Abstract**

Electromagnetically controlled transport in microstructured fluids is of considerable interest in advanced thermofluidic and microfluidic technologies, particularly when heat and mass transfer are strongly coupled. This study investigates steady micropolar fluid flow and coupled thermo-solutal transport in a transpiration-controlled channel driven by an upper Riga plate. The mathematical model accounts for non-uniform Riga-induced Lorentz forcing, thermal radiation, Joule dissipation, and Soret–Dufour cross-diffusion effects, leading to a highly nonlinear system of coupled boundary-value equations. The novelty of the work lies in examining the combined influence of these mechanisms within a confined micropolar channel configuration, which has received limited attention in the existing literature. The governing equations are transformed into a dimensionless form and solved using a fourth-order Hybrid Block Runge–Kutta shooting scheme with analytical initialization. The results demonstrate that micropolar material parameters suppress the velocity, microrotation, and concentration fields while enhancing the temperature distribution. Stronger electromagnetic forcing generated by the Riga plate and larger modified Hartmann effects significantly attenuate the flow and microrotation characteristics. Moreover, Dufour and Soret cross-diffusion mechanisms substantially modify thermal and concentration transport, whereas increasing thermal and mass Peclet numbers enhance local heat and mass transfer rates. These findings provide new insight into the control of coupled momentum, thermal, and species transport in electromagnetically actuated micropolar channel flows and offer useful guidance for the design of advanced thermal-management and microfluidic systems.

**Keywords**: Micropolar fluid; Riga plates; Soret–Dufour effects; HBM–RK4 Shooting Method; Radiation.

| Nomenclature | | | |
|---|---|---|---|
| $\rho$ | Fluid density ($kg\ m^{-3}$) | $\mu$ | Dynamic viscosity ($Kg.\ m^{-1}.\ s^{-1}$) |
| $u$ | Velocity in the x-direction ($m.\ s^{-1}$) | $\kappa$ | Vortex viscosity ($Kg.\ m^{-1}.\ s^{-1}$) |

| | | | |
|---|---|---|---|
| v | Velocity in the y-direction ($m.\ s^{-1}$) | γ | Spin-gradient viscosity ($Kg.\ m.\ s^{-1}$) |
| N | Microrotation ($s^{-1}$) | j | Microinertia density ($Kg.\ m$) |
| p | Pressure ($Kg.\ m^{-1}.\ s^{-2}$) | $\vec{B}$ | Magnetic field ($Kg.\ s^{-2}.\ A^{-1}$) |
| d | The magnets and the electrode width ($m$) | $c_p$ | Specific heat ($m^2.\ s^{-2}.\ K^{-1}$) |
| $D^*$ | mass diffusivity ($m^2.\ s^{-1}$) | $D_s$ | Soret coefficient ($m^2.\ s^{-1}$) |
| $D_e$ | Dufour coefficient ($m^2.\ s^{-1}$) | $K_T$ | Thermal diffusion ratio |
| $D_m$ | Mass diffusivity ($m^2.\ s^{-1}$) | $T_m$ | Mean temperature ($K$) |
| $\sigma$ | Electrical conductivity ($A^2.\ s^3.\ kg^{-1}.\ m^{-3}$) | $C_s$ | Mean concentration ($kg\ m^{-3}$) |
| $B_0$ | Magnetic field strength ($Kg.\ s^{-2}.\ A^{-1}$) | $T_w$ | Wall temperature ($K$) |
| $q_r$ | Radiative heat flux ($Kg.\ s^{-3}$) | $C_w$ | Wall concentration ($kg\ m^{-3}$) |
| x | Axial coordinate ($m$) | $k^*$ | Mean absorption coefficient ($m^{-1}$) |
| y | Transverse coordinate ($m$) | η | Dimensionless transverse coordinate |
| h | Channel half-width ($m$) | ψ | Stream function ($m^2\ s^{-1}$) |
| T | Temperature($K$) | f(η) | Dimensionless axial velocity profile |
| C | Species concentration ($kg\ m^{-3}$) | g(η) | Dimensionless microrotation profile |
| $\sigma^*$ | Stefan–Boltzmann constant ($kg\ s^{-3}\ K^{-4}$) | θ(η) | Dimensionless temperature profile |
| K | Coupling parameter | ϕ(η) | Dimensionless concentration profile |
| G | Spin-gradient viscosity parameter | Z | Modified Hartmann number |
| Re | Reynolds number | $R_d$ | Radiation parameter |
| Pr | Prandtl number | M | Magnetic parameter |
| $Pe_h$ | The thermal Peclet number | $E_c$ | Eckert number |
| $Pe_m$ | The mass Peclet number | Du | Dufour number |
| Sc | Schmidt number | $S_r$ | Soret number |
| $q_w$ | Wall heat flux ($Kg.\ s^{-3}$) | $Nu_x$ | Local Nusselt number |
| $\tau$ | Shear stress ($Kg.\ m^{-1}.\ s^{-2}$) | $Sh_x$ | Local Sherwood number |
| F | Lorentz force per unit volume ($Kg.\ m^{-2}.\ s^{-2}$) | | |



## 1. Introduction

Micropolar fluids, characterized by micro-rotational inertia and couple stresses, address the inherent limitations of the classical Navier–Stokes equations in modeling microstructured continua. Eringen's mathematical framework [1] provides a rigorous foundation for such media, with broad relevance to polymeric suspensions, liquid crystals, and biological flows. Prior investigations have extensively explored micropolar transport under conventional configurations, including thermal boundary layers over translating surfaces (Bhargava & Takhar [2]), unsteady MHD flows with Hall and ion-slip effects (Anika et al. [3]), nonlinear stretching-sheet dynamics (Bhargava et al. [4]; Takhar et al. [5]), and variable-property convection (Bhargava & Rana [6]), alongside comprehensive analyses in porous channel geometries [7–9]. Despite these advances, existing literature predominantly relies on symmetric geometries and uniform magnetic field assumptions, largely overlooking the nonlinear mathematical coupling between micro-rotation dynamics and spatially decaying electromagnetic forcing. Specifically, the theoretical gap concerning asymmetric Riga-induced Lorentz actuation—simultaneously integrated with wall transpiration and thermo-solutal cross-diffusion in confined micropolar channels—remains unaddressed, motivating the present unified analytical–numerical formulation.

The Soret and Dufour cross-diffusion mechanisms—wherein temperature gradients drive mass flux, and concentration gradients induce heat flux—play a critical role in coupled thermo-solutal transport processes relevant to chemical reactors, polymer processing, advanced materials manufacturing, and biomedical systems [10–15]. Within the micropolar fluid framework, these effects introduce additional nonlinear coupling between the energy and concentration equations, significantly enriching the mathematical structure of the governing boundary-value problem. Prior studies have examined Soret–Dufour interactions in diverse configurations, including porous cavities with partial heating (Alrige et al. [16]), anisotropic porous tubes with differential thermal boundaries (Ketchate et al. [17]), magnetized porous enclosures with power-law rheology (Hussain et al. [18]), stretching cylinders with thermal radiation (Salahuddin et al. [19]), complex geometries solved via lattice Boltzmann methods (Mohammadi & Nassab [20]), sensor-surface flows with activation energy (Awais et al. [21]), vertically stretched electrically conducting nanofluids with slip conditions (Seid et al. [22]), and Maxwell nanofluids over heated surfaces (Li et al. [23]). However, these investigations have largely treated cross-diffusion within Newtonian or simplified non-Newtonian contexts under conventional magnetic fields or symmetric geometries. The present work uniquely integrates Soret–Dufour coupling with asymmetric Riga-induced electromagnetic forcing and micropolar micro-rotation dynamics in a transpiration-controlled channel—a configuration that generates a distinct nonlinear interaction between electromagnetic actuation, microstructural rotation, and thermo-solutal transport, thereby addressing a previously unexplored theoretical gap in multi-physics micropolar flow modeling.



Magneto-hydrodynamic effects significantly influence flow and thermal transport in high-temperature engineering processes such as polymer extrusion and materials processing, where electromagnetic fields interact with electrically conducting microstructured fluids. Within the micropolar framework, prior investigations have addressed MHD transport over stretching surfaces with variable thermal conductivity (Mahmoud [24]), uniform free-stream convection (Abo-Eldahab & Ghonaim [25]), complex wavy porous channels with Joule heating and variable electrical conductivity [26]. Related studies on advanced non-Newtonian and nanofluid transport have explored tangent hyperbolic magnetohydrodynamic Darcy–Forchheimer Williamson hybrid nanofluid flow with variable thermal conductivity [27], radiative MHD Williamson nanofluid flow through Darcy–Forchheimer porous media in the presence of heat generation, activation energy, and motile microorganisms [28], and Yamada–Ota model-based Casson quadra hybrid nanofluid stagnation flow over an exponentially stretched cylinder incorporating Ohmic heating, internal heat generation, and Newtonian heating [29]. Additional investigations have considered non-

Darcian flow with radiation and Soret diffusion (Mabood et al. [30]), and partial-slip MHD convection with radiative Joule heating (Ramzan et al. [31]). While these studies provide valuable insights into uniform or conventionally applied magnetic fields, they do not capture the distinct mathematical structure arising from spatially decaying, asymmetric Lorentz forcing generated by a Riga plate. The present work uniquely bridges this gap by coupling micropolar micro-rotation dynamics with Riga-induced electromagnetic actuation in a transpiration-controlled asymmetric channel, thereby revealing new nonlinear interactions between electromagnetic forcing, microstructural effects, and cross-diffusion mechanisms that are absent in conventional MHD micropolar analyses.

The integration of MHD effects with micropolar fluid models offers significant advantages in advanced lubrication systems—such as nuclear reactor components, aerospace mechanisms, and magnetic storage devices—where classical models fail to capture microstructural and electromagnetic interactions. Studies by Naduvinamani & Shridevi [32] and Halambi & Hanmagowda [33] clarified the influence of surface roughness and Hartmann number on squeeze-film performance, while Hayat et al. [34] employed homotopy-based similarity solutions for MHD squeezing flow between parallel disks, and Bhattacharjee et al. [35] demonstrated substantial improvements in load capacity and thermal efficiency using micropolar lubricants in porous journal bearings. However, these investigations predominantly address symmetric configurations under uniform magnetic fields and conventional boundary conditions. The present work diverges fundamentally by examining asymmetric micropolar flow under spatially decaying Riga electromagnetic forcing in a transpiration-controlled channel, thereby introducing a distinct nonlinear coupling between micro-rotation dynamics and non-uniform Lorentz actuation that is absent in prior lubrication-oriented MHD micropolar analyses.



Recent investigations have also explored magnetic and thermal effects in related configurations. For instance, Ouyang et al. [36] examined heat generation and magnetic effects on unsteady ternary nanofluid flow over a dynamic wedge in porous media, while their subsequent stability analysis [37] addressed unsteady ternary nanofluid flow past a stretching/shrinking wedge with viscous dissipation and ohmic heating. Although these studies focus on nanofluid systems and wedge geometries, they underscore the broader relevance of electromagnetic forcing and thermal transport mechanisms in complex flow configurations, complementing the present micropolar Riga-channel analysis.

The numerical procedure employed in this study is based on converting the higher-order boundary value problem (BVP) into a first-order system. The unknown initial conditions (derivatives) are treated as shooting parameters and iteratively corrected using Newton's method. The resulting initial value problem (IVP) is solved using a high-order Runge–Kutta (RK) block scheme. The main idea of the shooting–Newton framework for nonlinear two-point BVPs is described in [38, 39]. Recently, a modern study based on the shooting method combined with RK scheme and

Newton correction for satisfying terminal boundary conditions is presented in [40]. In addition, the hybridization of shooting techniques with high-order RK schemes has recently been proposed in [41] to demonstrate the effectiveness of combining adaptive RK methods with iterative correction of missing initial conditions in solving BVPs. The RK4 scheme has local truncation error $O(h^5)$ and global error $O(h^4)$. So, implementing it in block-vector form guarantees consistent propagation of local errors across all components. This maintains stability and fourth-order accuracy for strongly coupled systems [42].

Accurate modeling of asymmetric micropolar fluid flow in electromagnetically actuated confined channels remains a mathematically challenging and physically underexplored problem. While prior studies have examined micropolar rheology, conventional magnetohydrodynamics, or cross-diffusion mechanisms in isolation, they predominantly rely on symmetric geometries and uniform magnetic fields, thereby neglecting the intricate nonlinear coupling between micro-rotation dynamics, spatially decaying Lorentz forcing, wall transpiration, and thermo-solutal transport. To address this critical theoretical gap, the present study develops a unified mathematical framework for asymmetric micropolar flow in a transpiration-controlled Riga channel, simultaneously incorporating radiative Joule dissipation and Soret–Dufour cross-diffusion effects. The significance of this work lies in its explicit resolution of the nonlinear interaction between microstructural rotation and non-uniform electromagnetic actuation—a coupling that fundamentally alters near-wall momentum, thermal, and concentration gradients. By integrating these multi-physics mechanisms within a single governing system, the study advances the mathematical understanding of complex transport phenomena and provides a robust computational foundation for advanced thermofluidic and micro-scale applications.

**The novelty of the present investigation is threefold:**

- It presents the first unified treatment of asymmetric micropolar flow under Riga-induced electromagnetic actuation, simultaneously accounting for wall transpiration, radiative Joule heating, and Soret–Dufour cross-diffusion.
- It explicitly analyzes the nonlinear coupling between micropolar micro-rotation dynamics and spatially decaying Lorentz forcing in confined asymmetric channels, revealing distinct transport behaviors absent in conventional MHD models.
- It introduces a high-order Hybrid Block Runge–Kutta shooting scheme combined with analytical initialization, specifically tailored to ensure stable convergence and numerical accuracy for strongly coupled nonlinear boundary-value problems of this class.

**To guide the present investigation, the following key research questions are explicitly addressed:**

i. How does the spatially decaying Lorentz forcing from the Riga plate reshape the coupled momentum, thermal, and concentration boundary layers in an asymmetric micropolar channel?
ii. To what extent do micropolar material parameters and wall transpiration modulate micro-rotation dynamics and effective flow resistance?
iii. How do Soret–Dufour cross-diffusion mechanisms interact with radiative Joule dissipation to influence near-wall heat and mass transfer rates?
iv. Can the proposed hybrid analytical-initialization shooting framework ensure robust convergence and numerical stability for this strongly coupled nonlinear boundary-value problem?

In particular, the present study is relevant to electromagnetic flow control and thermal management in advanced microfluidic and engineering systems. The results may be applied in the design of Riga-plate-based flow control devices, polymer processing technologies, cooling systems in high-temperature environments, and microfluidic transport systems where precise control of heat and mass transfer is required. The interaction between micropolar effects, radiation, and cross-diffusion mechanisms provides useful insight for optimizing performance in such applications.

## 2. Problem Definition and Governing Equations

This study investigates the steady laminar flow of a micropolar fluid through a two-dimensional channel of width $2h$, bound by parallel walls at $y = \pm h$ (Fig. 1). The channel walls allow uniform transverse mass flux, where fluid is injected or withdrawn at a constant speed $V_0$. Thermal and solutal gradients are established by maintaining the lower wall at temperature $T_1$ and solute concentration $C_1$, and the upper wall at $T_2$ and $C_2$. The upper wall is designed as an electromagnetic Riga plate, generating a streamwise Lorentz force that modulates the flow without mechanical contact. The micropolar fluid exhibits microstructural complexity, with internal particle spin coupled to macroscopic motion. Transport phenomena are influenced by thermal radiation, Joule heating, viscous dissipation, Soret–Dufour cross-diffusion, and a first-order chemical reaction. To solve the resulting strongly nonlinear coupled system, we employ Least Squares-based analytical initialization to construct physically consistent trial functions, which are then used as initial guesses for a Hybrid Block fourth-order Runge–Kutta shooting method, ensuring rapid convergence and high-fidelity solutions.

Assumptions underlying the model:

- The flow is steady, laminar, and two-dimensional.
- The channel walls permit uniform transverse injections or suction at a constant velocity $V_0$.

- The upper wall acts as a Riga plate, producing a streamwise Lorentz force; the lower wall is passive.
- The fluid is micropolar, with micro-rotation of particles coupled to the macroscopic flow.
- Transport is affected by thermal radiation, Joule heating, viscous dissipation, and cross-diffusion (Soret–Dufour) effects.
- A first-order chemical reaction occurs within the fluid.
- Boundary conditions for temperature and concentration are constant at the walls ( $T_1, C_1$ at the lower wall; $T_2, C_2$ at the upper wall).
- The solution method assumes physically consistent trial functions for initialization of the Hybrid Block Runge–Kutta shooting scheme.

The fundamental conservation laws for micropolar fluid flow—continuity, linear momentum, angular momentum, energy, and species transport—are expressed in their general three-dimensional form as follows, incorporating the microstructural coupling between particle spin and macroscopic motion [1,43]:



| | |
|---|---|
| $\frac{\partial \rho}{\partial t} + \nabla.(\rho\vec{V}) = 0,$ | (1) |
| $\rho\frac{D\vec{V}}{Dt} = -\nabla p + (\mu + k)\nabla^2\vec{V} + k(\nabla \times \vec{N}) + \vec{F}_{Lorentz}$ | (2) |
| $\rho j\frac{D\vec{N}}{Dt} = -k(2\vec{N} + \nabla \times \vec{V}) + \gamma\nabla^2\vec{N}$ | (3) |
| $\rho C_p(\vec{V}.\nabla T) = \nabla.(k_1\nabla T) + \underbrace{\sigma(\vec{V} \times \vec{B})^2}_{\text{Joule heating}} + \underbrace{\Phi}_{\text{Viscous dissipation}} - \nabla.\vec{q}_r + \underbrace{\frac{D_e k_T}{C_s}\nabla^2 C}_{\text{Dufour Effect}},$ | (4) |
| $\vec{V}.\nabla T = D^*\nabla^2 C + \underbrace{\frac{D_e k_T}{T_m}}_{\text{Soret Effect}}\nabla^2 T.$ | (5) |

In the governing system, $\rho$ is density, $\vec{V}$ velocity, $\vec{N}$ microrotation, $p$ pressure, $\mu$ dynamic viscosity, $\kappa$ vortex viscosity (micropolar coupling), $\gamma$ spin gradient viscosity, $j$ microinertia, $C_p$ specific heat, $k_1$ thermal conductivity, $D^*$ mass diffusivity, $\sigma$electrical conductivity, $\vec{B}$ magnetic field, $\vec{q}_r$ radiative heat flux, $D_e$ Dufour coefficient, $D_s$ Soret coefficient, $k_T$ thermal diffusion ratio, $T_m$ mean temperature, and $C_s$ mean concentration; the terms $\sigma(\vec{V} \times \vec{B})^2$and $\Phi$ represent Joule heating and viscous dissipation, respectively, while $-\nabla\cdot\vec{q}_r$ accounts for thermal radiation, $\frac{D_e k_T}{C_s}\nabla^2 C$ models the Dufour effect in energy transport, and $\frac{D_s k_T}{T_m}\nabla^2 T$ describes the Soret effect in species diffusion.

The dimensional governing equations for steady micropolar flow in a two-dimensional channel with transpiration-controlled walls are presented below, incorporating electromagnetic actuation, radiative heat transfer, dissipative heating, and Soret–Dufour coupling [44,45]:

$$\frac{\partial u}{\partial x} + \frac{\partial v}{\partial y} = 0, \tag{6}$$

$$\rho\left(u\frac{\partial u}{\partial x} + v\frac{\partial u}{\partial y}\right) = -\frac{\partial P}{\partial x} + (\mu + k)\left(\frac{\partial^2 u}{\partial x^2} + \frac{\partial^2 u}{\partial y^2}\right) + k\frac{\partial N}{\partial y} - \sigma B_0^2 u + \frac{\pi j_0 M_0}{8}\exp\left(-\frac{\pi}{b}y\right) \tag{7}$$

$$\rho\left(u\frac{\partial v}{\partial x} + v\frac{\partial v}{\partial y}\right) = -\frac{\partial P}{\partial y} + (\mu + k)\left(\frac{\partial^2 v}{\partial x^2} + \frac{\partial^2 v}{\partial y^2}\right) - k\frac{\partial N}{\partial x}, \tag{8}$$

$$\left(u\frac{\partial N}{\partial x} + v\frac{\partial N}{\partial y}\right) = -\frac{k}{j}\left(2N + \frac{\partial u}{\partial x} - \frac{\partial v}{\partial y}\right) + \frac{\nu_s}{j}\left(\frac{\partial^2 N}{\partial x^2} + \frac{\partial^2 N}{\partial y^2}\right), \tag{9}$$

$$\rho\left(u\frac{\partial T}{\partial x} + v\frac{\partial T}{\partial y}\right) = \frac{k_1}{C_p}\left(\frac{\partial^2 T}{\partial x^2} + \frac{\partial^2 T}{\partial y^2}\right) + \frac{\sigma}{C_p}B_0^2 u^2 + \frac{16\sigma^* T_\infty^{\,3}}{3k^* C_p}\left(\frac{\partial^2 T}{\partial y^2}\right) + \frac{D_e k_T}{C_p C_s}\left(\frac{\partial^2 C}{\partial y^2}\right), \tag{10}$$

$$\left(u\frac{\partial C}{\partial x} + v\frac{\partial C}{\partial y}\right) = D^*\left(\frac{\partial^2 C}{\partial x^2} + \frac{\partial^2 C}{\partial y^2}\right) + \frac{D_e k_T}{T_m}\left(\frac{\partial^2 T}{\partial y^2}\right). \tag{11}$$

In the dimensional formulation, $u$ and $v$ are the velocity components in the $x$- and $y$-directions, respectively; $T$ and $C$ are temperature and species concentration; the spin gradient viscosity is defined as $\nu_s = (\mu + \kappa/2)/j$; $\sigma$ is the electrical conductivity; $B_0$ is the applied magnetic field strength; and $\sigma^*$and $k^*$are the Stefan–Boltzmann constant and mean absorption coefficient, respectively, governing thermal radiation. The additional term $\frac{\pi j_0 M_0}{8}\exp\left(-\frac{\pi}{p}y\right)$ in the $x$-momentum equation represents an external electromagnetic body force generated by the Riga plate configuration.

The physically consistent boundary conditions for the system are specified as follows [45]:

$$y = -h: u = v = 0,\ N = -S\frac{\partial u}{\partial y}, T = T_1, C = C_1, \tag{12a}$$

$$y = +h: v = 0,\ u = \frac{v_0 x}{h},\ N = \frac{v_0 x}{h^2}, T = T_2, C = C_2. \tag{12b}$$

These boundary conditions enforce no-slip and transpiration-free flow at both walls, with micro-rotation governed by the parameter $S$, where $S = 0$ signifies rigid particle constraint, $S = 0.5$ reflects weak concentration with symmetric stress, and $S = 1$ mimics turbulent microrotation—while the upper wall's linearly varying velocity and micro-rotation profiles are induced by the electromagnetic actuation of the Riga plate configuration.

### 2.1. Dimensionless Formulation and reduction to a coupled ODE system

To enable analytical and numerical solutions, we reduce the two-dimensional governing system to a set of ordinary differential equations through similarity transformation. The following dimensionless variables are adopted [46]:

$$\eta = \frac{y}{h},\ \ \psi = -v_o x f(\eta),\ \ N = \frac{v_o x}{h^2} g(\eta),\ \ \theta(\eta) = \frac{T - T_2}{T_1 - T_2}, \phi(\eta) = \frac{C - C_2}{C_1 - C_2} \tag{13}$$

where $\eta$ is the scaled transverse coordinate, $\psi$ is the stream function (ensuring continuity identically), $f(\eta)$and $g(\eta)$ represent the dimensionless axial velocity and micro-rotation profiles, respectively, and $\theta(\eta)$, $\phi(\eta)$ denote the normalized temperature and concentration fields.

To capture the linear variation of wall temperature and concentration—where the upper wall conditions are $T_2 = T_1 - Ax$and $C_2 = C_1 - Bx$ with $A$ and $B$ as prescribed thermal and solutal gradients—we adopt a similarity transformation based on the stream function $\psi$, defined in the usual way:

$$u = \frac{\partial \psi}{\partial y}, \ v = -\frac{\partial \psi}{\partial x} \tag{14}$$

which yields the velocity components [46]:

$$u = -\frac{v_o x}{h} f'(\eta), \ v = v_o f(\eta) \tag{15}$$

Using (13)–(15) in the dimensional governing equations and simplifying leads to the following coupled system of nonlinear ordinary differential equations:

$$(1 + N_1)f''''(\eta) - N_1 g''(\eta) - R_e\big(f(\eta)f'''(\eta) - f'(\eta)f''(\eta)\big) - Mf''(\eta) - \frac{Zd}{R_e}\exp(-d\eta) = \tag{16}$$

$$N_2 g''(\eta) + N_1\big(f''(\eta) - 2g(\eta)\big) - N_3 R_e\big(f(\eta)g'(\eta) - f'(\eta)g(\eta)\big) = 0 \tag{17}$$

$$\left(1 + \frac{4}{3}R_d\right)\theta''(\eta) + P_{eh}\big(f'(\eta)\theta(\eta) - f(\eta)\theta'(\eta)\big) + P_r E_c(1 + N_1)f''(\eta)^2 + MP_r E_c f'( \\ + P_r D_u \phi''(\eta) = 0 \tag{18}$$

$$\phi''(\eta) + P_{em}(f'(\eta)\phi(\eta) - f(\eta)\phi'(\eta)) + S_r S_c \theta''(\eta) = 0 \quad (19)$$

Subject to the boundary conditions [44]:

$$\begin{gathered} \text{At } \eta = -1: \; f(-1) = f'(-1) = g(-1) = 0, \theta(-1) = \phi(-1) = 1, \\ \text{At } \eta = +1: f(1) = \theta(1) = \phi(1) = 0, \; f'(1) = -1, g(1) = 1. \end{gathered} \quad (20)$$

The boundary conditions at $\eta = \pm 1$ enforce no-slip and transpiration-free flow, micro-rotational compatibility with wall constraint, and prescribed thermal–solutal gradients: at the lower wall ($\eta = -1$), zero velocity and micro-rotation ($f(-1) = f'(-1) = g(-1) = 0$) reflect solid-wall adherence, while unit temperature and concentration ($\theta(-1) = \phi(-1) = 1$) correspond to the reference state $T_1, C_1$; at the upper wall ($\eta = +1$), vanishing temperature and concentration ($\theta(1) = \phi(1) = 0$) match the linearly varying wall conditions $T_2 = T_1 - Ax$, $C_2 = C_1 - Bx$, and the negative axial velocity gradient $f'(1) = -1$ along with unit micro-rotation $g(1) = 1$ are induced by the electromagnetic actuation of the Riga plate configuration.

The system is characterized by the coupling parameter $N_1 = \frac{\kappa}{\mu}$, the spin-gradient viscosity parameter $N_2 = \frac{\nu_s}{\mu h^2}$, the micro-inertia parameter $N_3 = \frac{j}{h^2}$, the Reynolds number $Re = \frac{v_0 h}{\nu}$ (positive for suction and negative for injection), the Prandtl number $Pr = \frac{\nu \rho C_p}{k_1}$, the Schmidt number $Sc = \frac{\nu}{D^*}$, the thermal Peclet number $Pe_h = Pr \cdot Re$, and the mass Peclet number $Pe_m = Sc \cdot Re$, the modified Hartmann number $Z = \frac{\pi j_0 M_0 h^4}{8 \rho \upsilon^2 x}$, the dimensionless parameters for the magnets and electrode width $d = \frac{\pi h}{p}$, radiation parameter $R_d = \frac{4\sigma^* T_\infty^3}{k^* k_1}$, the parameter of magnetic field $M = \frac{\sigma B_0^2 h^2}{\rho \upsilon}$, Eckert number $E_c = \frac{v_0^2 x^2}{C_p h^2 (T_1 - T_2)}$, Dufour number $Du = \frac{D_e k_T (C_1 - C_2)}{\upsilon C_p C_s (T_1 - T_2)}$ and Soret number $S_r = \frac{D_e k_T (T_1 - T_2)}{T_m (C_1 - C_2) \upsilon}$.

In the present study, the local Nusselt and Sherwood numbers serve as critical indicators of thermal and solutal transport efficiency across the channel, directly reflecting how electromagnetic actuation via the Riga plate, microstructural coupling, transpiration control, and cross-diffusion effects modulate the wall-normal gradients of temperature and concentration; elevated Nusselt values signify enhanced conductive heat removal—essential for thermal management in microfluidic cooling and lab-on-a-chip devices—while increased Sherwood numbers indicate intensified species diffusion, crucial for applications involving controlled drug delivery, chemical sensing, or reactive separation in bioengineered channels where wall concentration varies linearly with axial position. The dimensionless heat and mass transfer rates are defined respectively as:

| | |
|---|---|
| $Nu_x = \dfrac{xq''\|_{y=-h}}{k_1(T_1 - T_2)} = -\left(1 + \dfrac{4}{3}R_d\right)\theta'(-1),$ | (21) |
| $Sh_x = \dfrac{xm''\|_{y=-h}}{(C_1 - C_2)} = -\phi'(-1)$ | (22) |

where the local heat and mass fluxes are given by Fourier's and Fick's laws:

| | |
|---|---|
| $q'' = -k_1\left(\dfrac{\partial T}{\partial y}\right)\Big\|_{y=-h} - \dfrac{16\sigma^* T_\infty^3}{3k^*}\left(\dfrac{\partial T}{\partial y}\right)\Big\|_{y=-h}, \qquad m'' = -D^*\left(\dfrac{\partial C}{\partial y}\right)\Big\|_{y=-h}$ | (23) |

## 3. Numerical Method: Hybrid Block Runge–Kutta Shooting Method (Fourth Order)

The nonlinear mixed-order structure of the governing system makes the resulting boundary-value problem challenging to solve analytically. Therefore, the present study employs a Hybrid Block Runge–Kutta Shooting Method (fourth order), which combines classical Runge–Kutta integration with a shooting strategy to transform the boundary-value problem into a system of initial-value problems. This approach simplifies the numerical computation and avoids the direct solution of large coupled algebraic systems [38].

In this framework, the block Runge–Kutta scheme is applied to the full coupled vector system, allowing simultaneous advancement of all dependent variables within each computational step while preserving the nonlinear coupling structure of the governing equations [42]. In addition, a Newton-based shooting correction is utilized to iteratively satisfy the boundary conditions at the far boundary. The numerical results indicate rapid convergence of the iterative procedure to the prescribed tolerance, as shown in Table 3.

It is emphasized that the present approach is an implementation and adaptation of established numerical techniques rather than the development of a fundamentally new algorithm. The combination of RK4 integration, block formulation, and Newton-type correction provides a computational framework for handling strongly coupled nonlinear boundary-value problems. Semi-analytical methods such as HAM and VIM are based on series representations and may require the selection of convergence-control parameters. In contrast, the present study employs a direct numerical implementation based on RK4 integration and shooting techniques [47].

Consequently, the adopted Hybrid Block Runge–Kutta shooting framework provides a computational approach based on well-established numerical components for solving of the present high-order nonlinear boundary-value system.

To apply the RK4 scheme, the system is rewritten as a first-order system by introducing auxiliary variables for all derivatives up to third order for $f$ and first order for $g$, $\theta$, and $\phi$ as follows:

| | |
|---|---|
| $y_1 = f,\ y_2 = f',\ y_3 = f'',\ y_4 = f''',$ | (24) |
| $y_5 = g,\ y_6 = g',$ | (25) |
| $y_7 = \theta.\ y_8 = \theta',$ | (26) |
| $y_9 = \phi,\ y_{10} = \phi'.$ | (27) |

The original ODEs are then converted to:

| | |
|---|---|
| $y_1' = y_2,$ | (28) |
| $y_2' = y_3,$ | (29) |
| $y_3' = y_4,$ | (30) |
| $y_4' = f^{(4)},$ | (31) |
| $y_5' = y_6,$ | (32) |
| $y_6' = g'',$ | (33) |
| $y_7' = y_8,$ | (34) |
| $y_8' = \theta'',$ | (35) |
| $y_9' = y_{10},$ | (36) |
| $y_{10}' = \phi''$ | (37) |

The resulting system is:

| | |
|---|---|
| $Y' = F(\eta, Y),\ \ Y = (y_1, y_2, \ldots, y_{10})^T$ | (38) |

At $\eta = -1$, we only know$f,\ f', g,\ \theta,$ and $\phi$ while $f'', f''',\ g',\ \theta',\ \phi'$ are unknown**.**

Let $P = \left(f''(-1),\ f'''(-1),\ \ g'(-1),\ \theta'(-1),\ \phi'(-1)\ \ \right)$ be the vector of missing unknown initial conditions.

The goal is to determine $P$ such that, after integrating from $\eta = -1$ to $\eta = 1$, the right boundary conditions are satisfied.

This converts the BVP to a nonlinear algebraic system**:**

$$R(p) = \begin{pmatrix} f(1;p) - 0 \\ f'(1;p) + 1 \\ g(1;p) - 1 \\ \theta(1;p) - 0 \\ \phi(1;p) - 0 \end{pmatrix} = 0. \tag{39}$$

For a given trial vector $p^{(K)}$, we integrate the IVP from $\eta = -1$ to $\eta = 1$ using a fourth-order hybrid block RK method, where each step uses the four classical RK stages to obtain $Y(1;\, p^{(K)})$. Compute the residual $R(p^{(K)})$, and correct the missing initial conditions using the Newton iteration with finite-difference Jacobian updates:

$$p^{(K+1)} = p^{(K)} - J^{-1}(p^{(K)})\, R(p^{(K)}) \tag{40}$$

Equation (40) is used to update the shooting vector **P** until the residual norm falls below a prescribed tolerance, where $J$ is the Jacobian matrix. The Iterations continue until the convergence vector $P^*$ is obtained. Once the optimal vector $P^*$ is obtained, the system is solved to obtain accurate numerical approximations of $f, g, \theta$, and $\phi$, which satisfy all boundary conditions. This method provides a useful numerical framework for investigating the effects of different model parameters on the system dynamics. The presented system is reduced to the system proposed in [45] when $M = Z = d = E_c = R_d = S_c = S_r = D_u = P_r = 0$. A comparison between the numerical results obtained by the HBM–RK4 shooting method and the numerical results of LSM, HAN, and Modified AGM methods [45,48] is shown in table 1 and table 2 in order to validate our results.

**Table 1.** Comparison between the HBM and LSM results for $f(\eta)$, $g(\eta)$, $\theta(\eta)$ and $\phi(\eta)$ when $N_1 = N_2 = N_3 = Re = P_{eh} = P_{em} = 1, M = Z = d = E_c = R_d = S_c = S_r = D_u = P_r = 0$.

| $\eta$ | $f(\eta)$ | | $g(\eta)$ | | $\theta(\eta)$ | | $\phi(\eta)$ | |
|---|---|---|---|---|---|---|---|---|
| | LSM [45] | HBM | LSM [45] | HBM | LSM [45] | HBM | LSM [45] | HBM |
| -1.0 | 0.0000000 | 0.0000000 | 0.0000000 | 0.0000000 | 1.0000000 | 1.0000000 | 1.0000000 | 1.000000 |
| -0.8 | 0.0174687 | 0.0174779 | 0.0396698 | 0.0396770 | 0.9416591 | 0.9416673 | 0.9416591 | 0.9416673 |
| -0.6 | 0.0622842 | 0.0622960 | 0.0548281 | 0.0548376 | 0.8770842 | 0.8770994 | 0.8770842 | 0.8770994 |
| -0.4 | 0.1229596 | 0.0122967 | 0.0579423 | 0.0579516 | 0.8022456 | 0.8022538 | 0.8022456 | 0.8022538 |
| -0.2 | 0.1878851 | 0.1878945 | 0.0607437 | 0.0607528 | 0.7151699 | 0.7151795 | 0.7151699 | 0.7151795 |
| 0.0 | 0.2453483 | 0.2453571 | 0.0754995 | 0.0755052 | 0.6156695 | 0.6156793 | 0.6156695 | 0.6156793 |
| 0.2 | 0.2834991 | 0.2835075 | 0.1163682 | 0.1163769 | 0.5049537 | 0.5049617 | 0.5049537 | 0.5049617 |
| 0.4 | 0.2903495 | 0.2903579 | 0.2011074 | 0.2011170 | 0.3852542 | 0.3852610 | 0.3852542 | 0.385261 |
| 0.6 | 0.2537342 | 0.2537412 | 0.3532236 | 0.3532305 | 0.2593863 | 0.2593955 | 0.2593863 | 0.2593955 |
| 0.8 | 0.1612208 | 0.1612298 | 0.6047983 | 0.6048058 | 0.1302184 | 0.1302265 | 0.1302184 | 0.1302265 |
| 1.0 | 0.0000000 | 0.0000000 | 1.0000000 | 1.0000000 | 0.0000000 | 0.0000000 | 0.0000000 | 0.000000 |

**Table 2.** Comparison between the HBM, HAN and Modified AGM results for $f(\eta)$, $g(\eta)$, $\theta(\eta)$ and $\phi(\eta)$ when $R_d = E_c = d = Z = M = 0.8, P_{em} = 1, P_{eh} = Re = N_3 = N_2 = N_1 = S_c = S_r = D_u = P_r = 0$.

| $\eta$ | $f(\eta)$ | | | $g(\eta)$ | | |
|---|---|---|---|---|---|---|
| | HAN [48] | HBM | Modified AGM [48] | HAN [48] | HBM | Modified AGM [48] |
| -1.0 | 0.0000000 | 0.0000000 | 0.0000000 | 0.0000000 | 0.0000000 | 0.0000000 |
| -0.8 | 0.0174779 | 0.0174779 | 0.0174381 | 0.0396770 | 0.0396770 | 0.0401197 |
| -0.6 | 0.0622960 | 0.0622960 | 0.0622887 | 0.0548376 | 0.0548376 | 0.0552135 |
| -0.4 | 0.1229673 | 0.1229673 | 0.1229839 | 0.0579516 | 0.0579516 | 0.0580888 |
| -0.2 | 0.1878944 | 0.1878945 | 0.1879272 | 0.0607528 | 0.0607528 | 0.0607716 |
| 0.0 | 0.2453571 | 0.2453571 | 0.2454000 | 0.0755051 | 0.0755052 | 0.0755700 |
| 0.2 | 0.2835075 | 0.2835075 | 0.2835573 | 0.1163768 | 0.1163769 | 0.1165027 |
| 0.4 | 0.2903579 | 0.2903579 | 0.2904144 | 0.2011168 | 0.2011170 | 0.2011824 |
| 0.6 | 0.2537412 | 0.2537412 | 0.2538058 | 0.3532303 | 0.3532305 | 0.3531528 |
| 0.8 | 0.1612298 | 0.1612298 | 0.1613049 | 0.6048056 | 0.6048058 | 0.6046823 |
| 1.0 | 0.0000000 | 0.0000000 | 0.0000000 | 1.0000000 | 1.0000000 | 1.0000000 |

**Table 3.** Convergence history of the Newton shooting procedure.

| **Iteration** | **Residual norm** |
|---|---|
| 1 | $1.947 \times 10^{0}$ |
| 2 | $4.117 \times 10^{-1}$ |
| 3 | $2.443 \times 10^{-3}$ |
| 4 | $2.530 \times 10^{-8}$ |

**Table 4.** Mesh-independence study of the HBM–RK4 shooting method.

| h | **Final Residual** | **Newton iterations** | **CPU times** |
|---|---|---|---|
| 0.0400 | $7.11 \times 10^{-7}$ | 1 | 0.0215 |
| 0.0200 | $5.84 \times 10^{-8}$ | 1 | 0.0302 |
| 0.0100 | $2.64 \times 10^{-8}$ | 1 | 0.0518 |
| 0.0050 | $2.54 \times 10^{-8}$ | 1 | 0.0929 |
| 0.0025 | $2.53 \times 10^{-8}$ | 1 | 0.1633 |
| 0.00125 | $2.53 \times 10^{-8}$ | 1 | 0.3446 |

To check whether the numerical implementation converges, we used Newton's method with a stopping tolerance of $10^{-6}$. Table 3 shows how the residuals evolve during the Newton shooting procedure. In four iterations, the residual norm drops from $1.947$ to $2.53 \times 10^{-8}$, which is below the prescribed tolerance of $10^{-6}$. This behavior illustrates that the Newton correction procedure converges rapidly when determining the missing initial conditions.

Table 4 presents a mesh-independence study for various step sizes. As the step size $h$ decreases, the final residual converges to approximately $2.53 \times 10^{-8}$. For step sizes $h \leq 0.01$, the residual remains nearly constant. This indicate that further mesh refinement has a very small influence on the numerical solution. Consequently, for the parameter values examined in this study, the numerical results can be considered as mesh-independent. In addition, the CPU time increases gradually as the mesh is refined, which is expected because more computations are required.

Together, the results in Tables 3 and 4 provide numerical evidence that the proposed implementation is both convergent and robust.

## 4. Results and discussion

In these numerical simulations, it is focused on the profiles of the stream function $f(\eta)$, the microrotation function $g(\eta)$, the temperature distributions $\theta(\eta)$, the concentration distributions $\phi(\eta)$ together with heat transfer rate $Nu_x$ and solutal transfer rate $Sh_x$. Several key factors are examined such as Reynolds number $Re$ $(0.5 \leq Re \leq 0.8)$, Pèclet number $P_{eh} = P_{em}$ $(0.4 \leq P_{eh} = P_{em} \leq 1.0)$, Dufour number $D_u$ $(0 \leq D_u \leq 5.0)$ , radiation number $R_d(0 \leq R_d \leq 5.0)$, magnetic field parameter $M$ $(0 \leq M \leq 5.0)$, and material parameters $N_1$, $N_2$and $N_3$ [45, 49].

Figures 2–5 display the features of $f(\eta)$, $g(\eta)$, $\theta(\eta)$, and $\phi(\eta)$under the impacts of the material parameters $N_1$, $N_2$and $N_3$, with equal values considered for these parameters alongside three different Reynolds numbers ($Re = 0.1, 0.3, 5$). The results indicate that increasing $N_1$, $N_2$and $N_3$causes a reduction in the profiles of the stream function $f(\eta)$, microrotation function $g(\eta)$, and concentration distributions $\phi(\eta)$, while the temperature distributions $\theta(\eta)$are enhanced. These profiles are more sensitive at lower $Re$, whereas at higher $Re$, the variations induced by $N_1$, $N_2$ and $N_3$become less pronounced, particularly for $\theta(\eta)$and $\phi(\eta)$. From a physical perspective, the material parameters $N_1$, $N_2$and $N_3$govern the micropolar characteristics of the fluid, namely microrotation viscosity, the coupling strength between linear and angular momentum, and micro-inertia effects. Increasing these parameters intensifies the internal microstructural resistance to both translational motion and particle spin, thereby suppressing the microrotation field $g(\eta)$ through enhanced couple-stress dissipation and reducing the stream function $f(\eta)$due to greater effective viscosity. This microstructurally induced drag also weakens convective transport near the wall, leading to a thinner concentration boundary layer and thus a diminished $\phi(\eta)$profile. Conversely, the reduction in convective heat removal, combined with enhanced viscous and micro-rotational dissipation, results in thermal boundary layer thickening and elevated $\theta(\eta)$values. The attenuated sensitivity at higher $Re$arises because inertial forces dominate over microstructural effects, partially masking the influence of $N_1$, $N_2$and $N_3$on the coupled transport structure. In a related context, **Figures 6-8** show the variations of Reynolds number $Re$, material parameters $N_1$, $N_2$,$N_3$ and Pèclet numbers $P_{eh}$,$P_{em}$ on the stream function $f(\eta)$, temperature distribution $\theta(\eta)$, and the concentration distribution $\phi(\eta)$. These illustrations are conducted at $M = 0.5,\ Z = 1,\ d = 0.5,\ E_c = 0.2,\ R_d = 0.4,\ S_c = S_r = 0.2,\ D_u = 0.4,\ P_r = 1$. Remarkably, increasing $N_1$, $N_2$,$N_3$, $Re$ and $P_{eh}$,$P_{em}$ (red curve) causes a reduction in the $f(\eta)$ while both of $\theta(\eta)$ and $\phi$

$(\eta)$ get higher values. As $N_1$, $N_2$,$N_3$, and $P_{eh}$,$P_{em}$ is increased and $Re$ is decreased $(Re = -0.5)$, more lower features of $f(\eta)$ are noted and $\theta(\eta)$ is improved. At $N_1$, $N_2$,$N_3 = Re = P_{eh}$,$P_{em} = 1.0$, lower improvements in the values of $f(\eta)$ and diminishing in $\theta(\eta)$ while a significant reduction in $\phi(\eta)$ are obtained compared to the previous case. The values where $N_1$, $N_2$,$N_3 = 0.05$, $Re = 0.6$,$P_{eh}$,$P_{em} = 0.6$ causes improvement values of $f(\eta)$ while both of $f(\eta)$ and $\theta(\eta)$ get lower values.

In **Figures 9-12,** the influences of the Reynolds number $Re$ where $-5.0 \le Re \le 15$ on the stream function $f(\eta)$, the microrotation function $g(\eta)$, the temperature distribution $\theta(\eta)$ together with the concentration distribution $\phi(\eta)$ are examined. These illustrations were referenced at at $N_1 = N_2 = N_3 = P_{eh} = P_{em} = 1$, $M = 0.5$, $Z = 1$, $d = 0.5$, $E_c = 0.2$, $R_d = 0.4$, $S_c = S_r = 0.2$, $D_u = 0.4$, $P_r = 1$. The results disclosed that the raising in Re causes a significantly reduction in both of $f(\eta)$ and $g(\eta)$ and a lower diminishing in features of temperature and concentration. Physically, the Reynolds number represents the ratio of inertial forces to viscous forces in the flow. As $Re$ increases, inertial effects become dominant, which suppresses the momentum diffusion caused by viscosity. Consequently, the fluid experiences a stronger resistance to rotational and shear-induced motion. That effect leads to a pronounced reduction in the stream function $f(\eta)$ and the microrotation profile $g(\eta)$. This behavior reflects the weakening of both translational and micro-rotational motions of the micropolar fluid as the flow becomes increasingly inertia dominated.

The impacts of varying $N_1$ where $0.1 \le N_1 \le 7$ on the microrotation function $g(\eta)$, and the temperature distribution $\theta(\eta)$ are examined with help of **Figures** 13 and 14. Remarkably, the growing $N_1$ causes that the fluid becomes more viscose which decreases the convective transport and enhances the dissipation effects and as results $g(\eta)$ is diminishing while $\theta(\eta)$ is improved. In a related context, **Figure 15** displays the variation impacts of $N_2$ on the microrotation function $g(\eta)$ indicating that a clear reduction in $g(\eta)$ as $N_2$ increases. Furthermore, **Figure 16** shows the influences of the alteration in $N_3$ on the microrotation function $g(\eta)$ at $N_1 = N_2 = P_{eh} = P_{em} = 1$, $M = 0.5$, $Z = 1$, $d = 0.5$, $E_c = 0.2$, $R_e = 1$, $R_d = 0.4$, $S_c = S_r = 0.2$, $D_u = 0.4$, $P_r = 1$. Noticeably, $g(\eta)$ get lower features as $N_3$ is raising due to the higher friction in the fluid layers.

**Figures 17 and 18** depict the profiles of the thermal Peclet number $Pe_h = Pr \cdot Re$ and the mass Peclet number $Pe_m = Sc \cdot Re$ on the temperature distribution $\theta(\eta)$ at $N_1 = N_2 = N_3 = P_{eh} = 1$, $M = 0.5$, $Z = 1$, $d = 0.5$, $E_c = 0.2$, $R_e = 1$, $R_d = 0.4$, $S_c = S_r = 0.2$, $D_u = 0.4$, $P_r = 1$. It is found that the growing in $Pe_h$ enhances the temperature distribution while $\theta(\eta)$ gets lower features as $Pe_m$ is altered. In the connected context, **Figure 19** shows the impacts of $Pe_m$ on the concentration distribution $\phi(\eta)$. The results revealed that the increase in $Pe_m$ gives higher features for $\phi(\eta)$. From the physical view, the thermal Peclet number $Pe_h$

quantifies the relative strength of convective heat transport compared to conductive heat diffusion. As $Pe_h$ is increasing, convective transport becomes more dominant; that allows thermal energy to be carried farther from the heated surface before it can diffuse away. As a result, the thermal boundary layer thickens and the temperature distribution $\theta(\eta)$ increases throughout the boundary layer. Conversely, increasing the mass Peclet number $Pe_m$ strengthens convective mass transport relative to molecular diffusion. A larger $Pe_m$ enhances the removal of heat through intensified solutal convection and cross-diffusion mechanisms, which indirectly suppresses the thermal field. Consequently, the temperature profile $\theta(\eta)$ exhibits lower magnitudes as $Pe_m$increases, indicating a thinning of the thermal boundary layer.

**Figures 20-23** depict the features of the stream function $f(\eta)$, the microrotation function $g(\eta)$, on the temperature distribution $\theta(\eta)$ and the concentration distribution $\phi(\eta)$ for varying of the magnetic field coefficient M and for several values of $Re$ and $P_{em}$. The results disclosed that the alteration in $M$ causes a higher Lorentz force results in a higher flow resistance and hence $f(\eta)$, $g(\eta)$ and $\theta(\eta)$ are diminishing. Conversely, the gradients of the temperature are enhanced which causes higher concentration distributions.

In the same context, **Figures 24–27** show the impacts of the modified Hartmann number $Z$on the profiles of $f(\eta)$, $g(\eta)$, $\theta(\eta)$and $\phi(\eta)$at $N_1 = N_2 = N_3 = P_{eh} = 1$, $M = 0.5$, $d = 0.5$, $E_c = 0.2$, $R_d = 0.4$, $S_c = S_r = 0.2$, $D_u = 0.4$, $P_r = 1$. Like the impacts of $M$, increasing $Z$ causes an obstruction to the flow and damping of the overall convection, which in turn reduces $f(\eta)$, $g(\eta)$and $\theta(\eta)$, while the values of $\phi(\eta)$are augmented due to the growing temperature gradients. Physically, the modified Hartmann number $Z$ quantifies the strength of spatially decaying Lorentz forcing generated by the Riga plate; as $Z$ increases, the electromagnetic body force acts opposite to the main flow direction near the active wall, directly suppressing fluid acceleration and, consequently, reducing the shear-induced micro-rotation $g(\eta)$ through weakened momentum–angular momentum coupling. Unlike conventional uniform-field MHD models where the magnetic damping is spatially constant, the Riga-induced forcing decays exponentially away from the wall, producing a highly localized modification of the boundary-layer structure that selectively attenuates near-wall velocity and microrotation while allowing the core flow to remain relatively unaffected. This asymmetric damping reshapes the coupled transport: the reduced convective removal of heat thickens the thermal boundary layer, yet the concurrent enhancement of temperature gradients near the wall intensifies the Soret-driven mass flux, thereby elevating $\phi(\eta)$. From an engineering perspective, $Z$thus serves as a non-mechanical control parameter for regulating near-wall shear, microrotation, and solutal gradients; in electromagnetic microfluidic actuators, adjusting $Z$enables precise modulation of flow resistance and coupled heat–mass transfer without moving parts, suggesting practical utility in targeted drug-delivery channels and lab-on-chip separation systems where spatially selective actuation is essential.

The impacts of the radiation parameter $R_d$, for several values of $R_e$ and $P_{em}$ on the stream function $f(\eta)$, the microrotation function $g(\eta)$, the temperature distribution $\theta(\eta)$ and the concentration distribution $\phi(\eta)$ at $N_1 = N_2 = N_3 = P_{eh} = Z = 1,\ M = 0.5, d = 0.5, E_c = 0.2, S_c = S_r = 0.2,\ D_u = 0.4, P_r = 1$ are illustrated in **Figures 28-31.** The raising in non-linear radiation parameter $R_d$ causes a lower reduction in profiles of $f(\eta)$, and $g(\eta)$, clear diminishing in $\theta(\eta)$ but the concentration $\phi(\eta)$ get higher behaviors. In facts the raising in $R_d$ leads to a higher gradient of the temperature and hence $\phi(\eta)$ is improved. In the same context, **Figures 32-34** depict the impacts of the variations of $Du$ on the stream function $f(\eta)$, the microrotation function $g(\eta)$ and concentration $\phi(\eta)$ at $N_1 = N_2 = N_3 = P_{eh} = Z = 1,\ M = 0.5, d = 0.5, R_d = 0.4, E_c = 0.2, S_c = S_r = 0.2, P_r = 1$. The features of $f(\eta)$, and $g(\eta)$ are decreased as Du is raising while a significant improvement in profiles of $\phi(\eta)$ is observed. Physically, the Dufour effect represents energy flux induced by concentration gradients, which introduces an additional coupling between mass diffusion and thermal transport mechanisms. As the Dufour number increases, a larger portion of the system's energy is redirected into concentration-driven heat flux rather than momentum transport. Consequently, the effective momentum diffusion weakens, leading to a reduction in both the velocity field $g(\eta)$ and the microrotation distribution $g(\eta)$. On the other hand, the enhanced cross-diffusion mechanism promotes mass transport, resulting in a noticeable augmentation in the concentration profile $\phi(\eta)$. In a related context, as can be seen from **Figures 35-38**, a reduction in the features of $f(\eta)$, $g(\eta)$, and $\theta(\eta)$ are oven as $S_r$ is altered while it causes a clear improvement in the profiles of $\phi(\eta)$. Furthermore, the heat and solutal transfer represented by the values of $Nu_x$ and $Sh_x$ for the variations of $Re$, thermal Peclet number $Pe_h$ and the mass Peclet number $Pe_m$ are displayed in **Figures 39-40.** It is noted that the alteration in Re causes an increase in the overall convection and hence both of $Nu_x$ and $Sh_x$. The gradients of the temperature and concentration are enhanced as $Pe_h$ and $Pe_m$ increases which in turn improves $Nu_x$ and $Sh_x$. All these observations are found at at $N_1 = N_2 = N_3 = Z = 1,\ M = 0.5, d = 0.5, R_d = 0.4, E_c = 0.2, S_c = S_r = 0.2, D_u = 0.4, P_r = 1$.

## 5. Conclusion

The present study addresses the emerging need for accurate modelling of coupled momentum, heat, and mass transport in microstructured fluids under active electromagnetic control, which is of significant relevance in modern microfluidic and thermal management systems. In particular, we investigate steady micropolar fluid flow in a confined channel subjected to Riga plate-induced spatially varying electromagnetic forcing, which provides a more realistic representation of non-uniform Lorentz actuation compared to classical uniform magnetic field models. The model further incorporates thermal radiation and Soret–Dufour cross-diffusion effects to capture the complex coupling between heat and mass transfer in microstructured media. To the best of the authors' knowledge, the combined interaction of these mechanisms in a transpiration-controlled micropolar channel has not been sufficiently explored in the existing literature. The governing nonlinear boundary-value problem is formulated in dimensionless form via similarity transformations and solved using a robust hybrid Block Runge–Kutta shooting method. The study systematically examines the influence of key physical parameters on the velocity, microrotation, temperature, and concentration fields. **Thus, the following key conclusions can be drawn from this study.**

- The micropolar material parameters significantly suppress the stream function, microrotation, and concentration fields, while enhancing the temperature distribution due to increased microstructural resistance and viscous dissipation effects.
- An increase in the Reynolds number leads to a pronounced reduction in both translational and rotational motions, reflected in lower values of $f(\eta)$ and $g(\eta)$, with comparatively weaker effects on temperature and concentration profiles.
- The thermal Peclet number enhances convective heat transport, resulting in a thicker thermal boundary layer and increased temperature distribution, whereas the mass Peclet number strengthens convective mass transport and enhances the concentration field while reducing the temperature response.
- Increasing $Pe_m$significantly augments the concentration profile $\phi(\eta)$,confirming the dominance of convective mass transport over molecular diffusion at higher values.
- The presence of a magnetic field and higher Hartmann number introduces Lorentz forces that resist fluid motion, resulting in reduced $f(\eta)$, and $\theta(\eta)$, while indirectly enhancing concentration through stronger thermal gradients.
- Thermal radiation effects reduce velocity, microrotation, and temperature distributions, while increasing concentration due to enhanced radiative heat transfer and steeper temperature gradients.
- The Dufour effect weakens momentum and microrotation fields but significantly enhances concentration, indicating strong coupling between heat and mass transfer mechanisms.
- Variations in the Soret number reduce velocity, microrotation, and temperature distributions but significantly enhance concentration, while higher $Re$, $Pe_h$, and $Pe_m$ collectively improve the local heat and mass transfer rates.

## 6. Limitations and Future Scope

Despite the comprehensive formulation and robust numerical treatment presented in this study, certain limitations should be acknowledged. First, the analysis is confined to a two-dimensional steady asymmetric flow configuration; transient effects and three-dimensional flow structures are not considered. Second, the micropolar model assumes constant thermophysical properties, whereas temperature-dependent viscosity, thermal conductivity, or magnetic permeability may influence the transport behavior in practical applications. Third, the electromagnetic actuation is modeled through an idealized Riga surface representation, neglecting possible edge effects, electrode spacing variations, and non-uniform field distributions that may arise in realistic devices. Additionally, nanoparticle aggregation, chemical reactions, or bio-physical interactions are beyond the scope of the present framework.

Future research may extend the current model to unsteady and three-dimensional configurations, incorporate variable property effects, and explore hybrid nanofluids or bio-micropolar fluids under more realistic electromagnetic boundary conditions. Experimental validation and the integration of machine-learning-assisted numerical acceleration techniques may further enhance predictive capability and practical applicability in advanced thermofluidic and micro-scale engineering systems.

**Acknowledgment**

The authors extend their appreciation to the Deanship of Research and Graduate Studies at King Khalid University for funding this work through the Large Research Project under grant number RGP2/107/47.

**Funding**

Deanship of Research and Graduate Studies at King Khalid University RGP2/107/47.

**Data availability**

All data generated or analysed during this study are included in this published article.



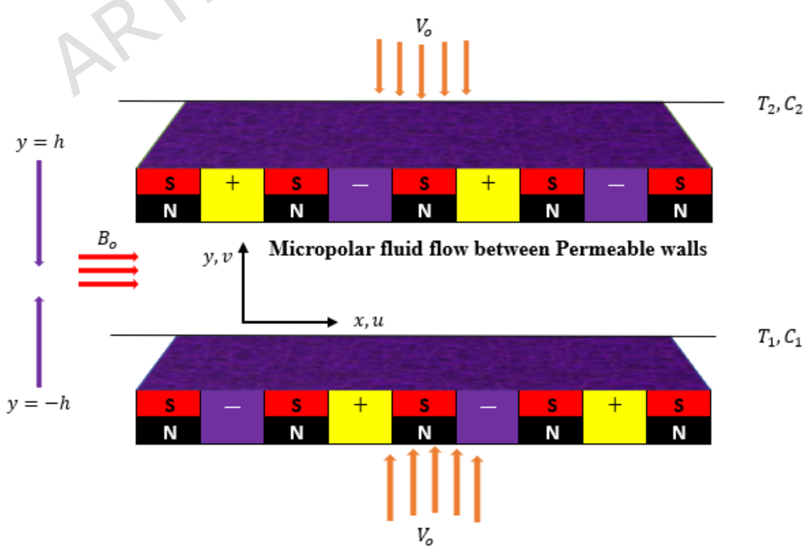


**Figure 1:** Schematic of micropolar fluid flow in a channel with transpiration-controlled walls and an upper Riga plate under linearly varying thermal and solutal wall conditions.

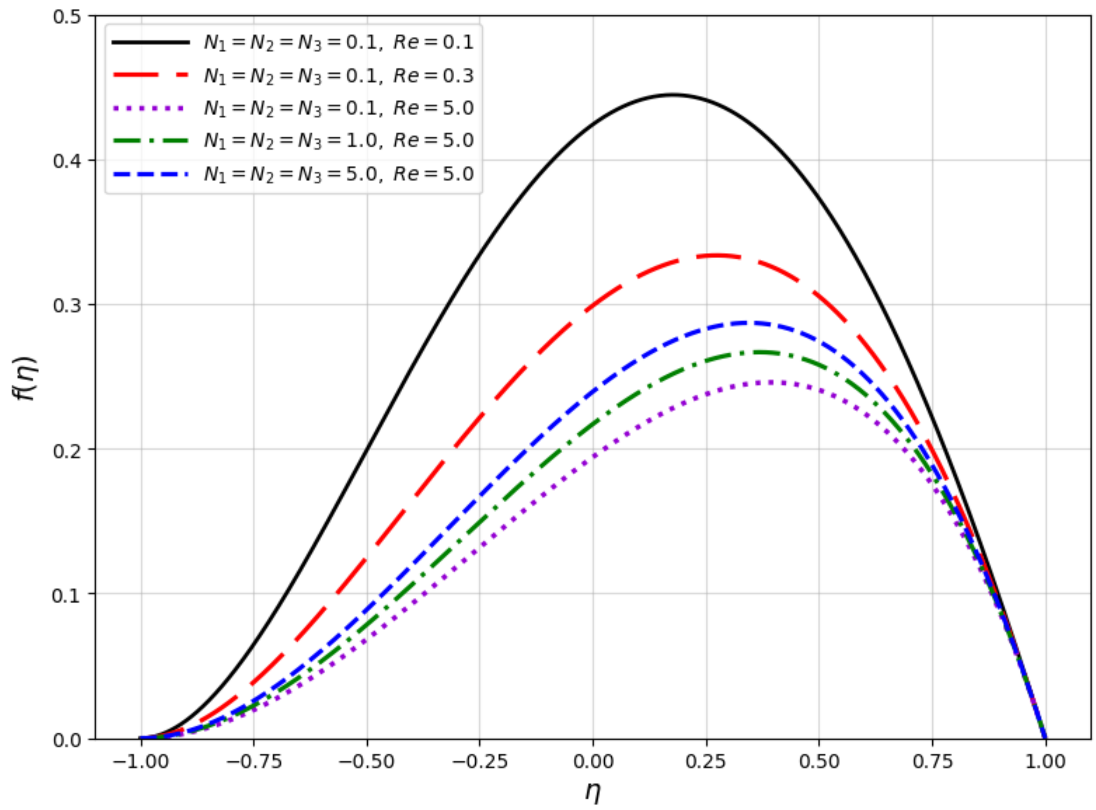


**Figure 2:** Effect of varying Reynolds number $Re$ and material parameters $N_1$, $N_2$ and $N_3$ on the stream function $f(\eta)$ at $P_{eh} = P_{em} = 1$, $M = 0.5$, $Z = 1$, $d = 0.5$, $E_c = 0.2$, $R_d = 0.4$, $S_c = S_r = 0.2$, $D_u = 0.4$, $P_r = 1$.



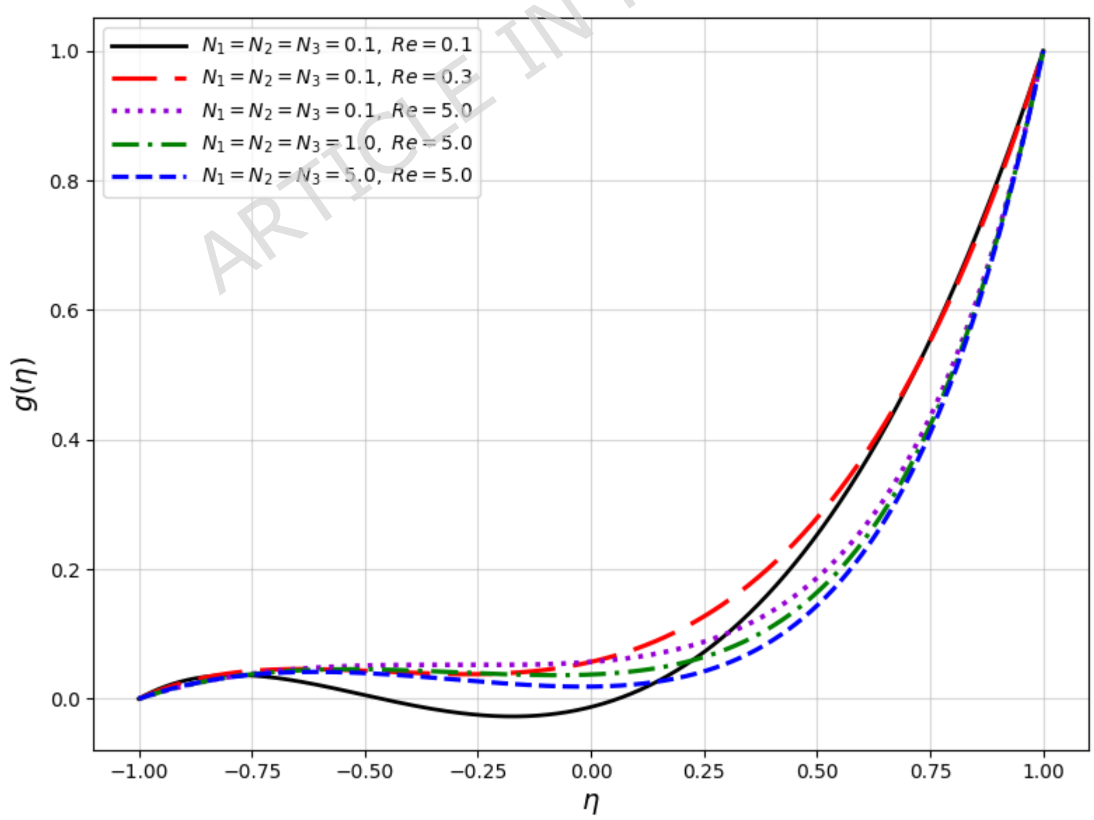


**Figure 3:** Effect of varying Reynolds number $Re$ and material parameters $N_1$, $N_2$ and $N_3$ on the microrotation function $g(\eta)$ at $P_{eh} = P_{em} = 1$, $M = 0.5$, $Z = 1$, $d = 0.5$, $E_c = 0.2$, $R_d = 0.4$, $S_c = S_r = 0.2$, $D_u = 0.4$, $P_r = 1$.

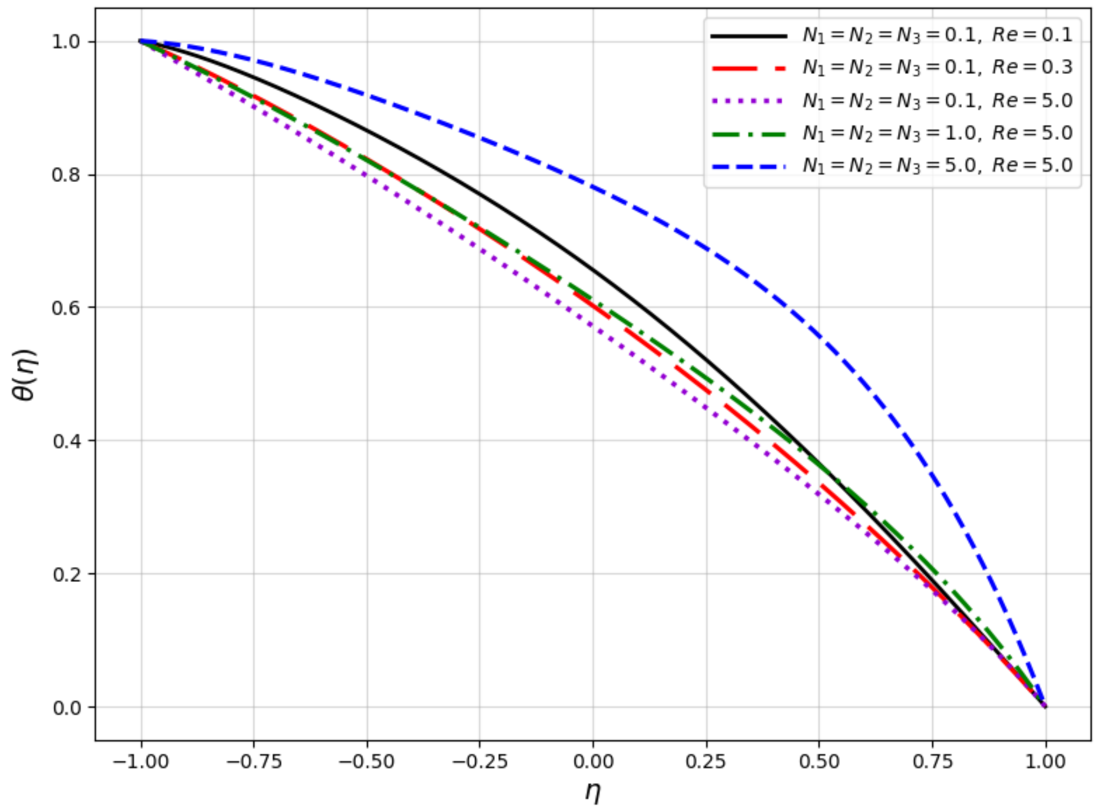


**Figure 4:** Effect of varying Reynolds number $Re$ and material parameters $N_1$, $N_2$and $N_3$ on the temperature distribution function $\theta(\eta)$ at $P_{eh} = P_{em} = 1$, $M = 0.5$, $Z = 1$, $d = 0.5$, $E_c = 0.2$, $R_d = 0.4$, $S_c = S_r = 0.2$, $D_u = 0.4$, $P_r = 1$.



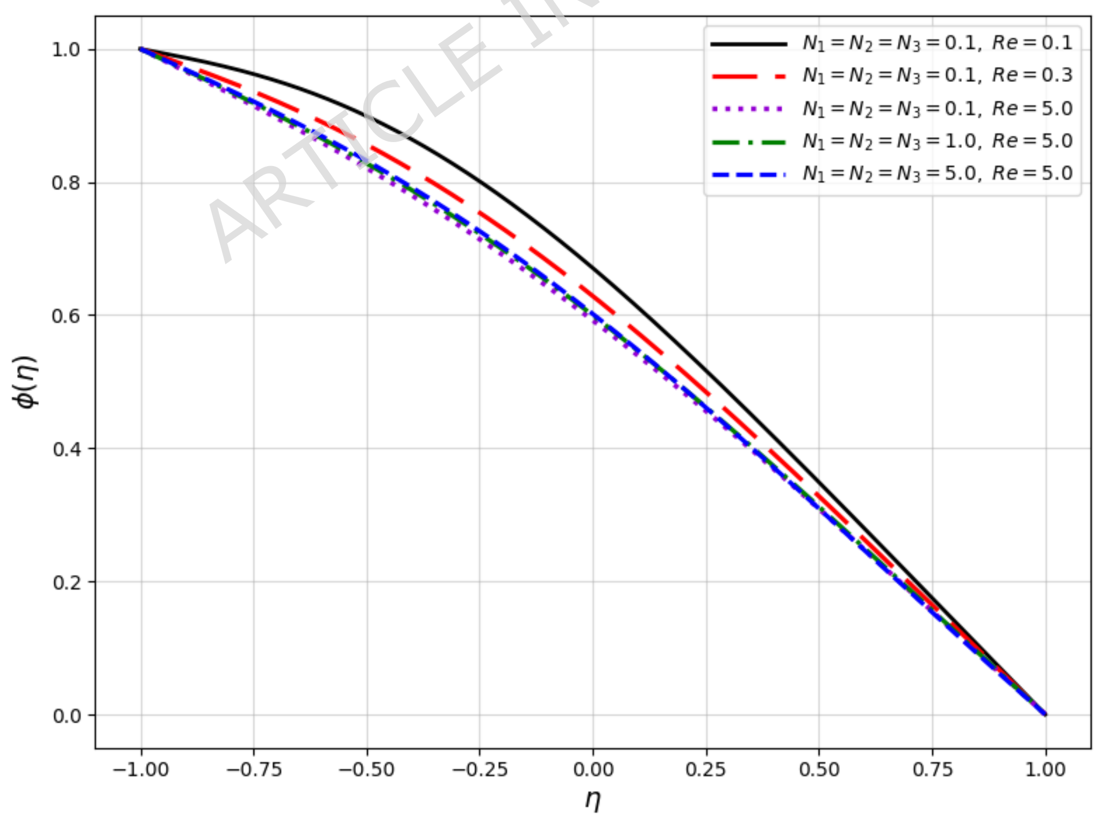


**Figure 5:** Effect of varying Reynolds number $Re$ and material parameters $N_1$, $N_2$and $N_3$ on the concentration distribution $\phi(\eta)$ at $P_{eh} = P_{em} = 1$, $M = 0.5$, $Z = 1$, $d = 0.5$, $E_c = 0.2$, $R_d = 0.4$, $S_c = S_r = 0.2$, $D_u = 0.4$, $P_r = 1$.

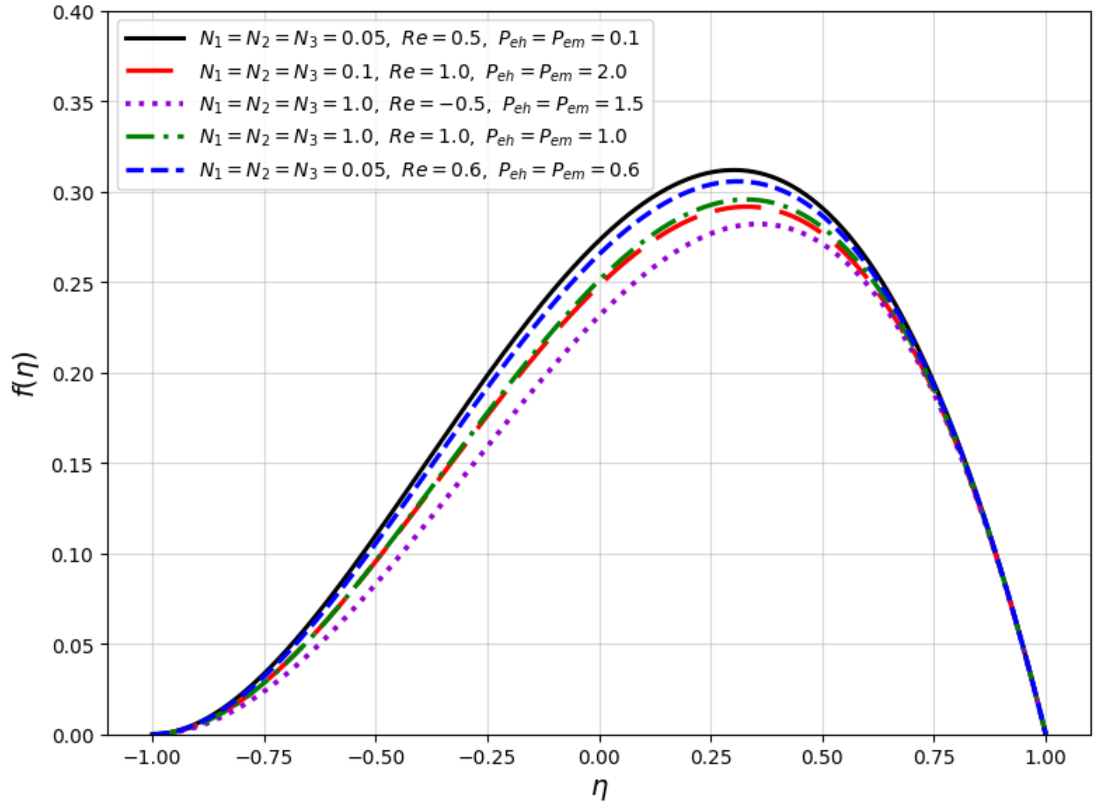


**Figure 6:** Effect of varying Reynolds number $Re$, material parameters $N_1$, $N_2$,$N_3$ and Peclet numbers $P_{eh}$,$P_{em}$ on the stream function $f(\eta)$ at $M = 0.5$, $Z = 1$, $d = 0.5$, $E_c = 0.2$, $R_d = 0.4$, $S_c = S_r = 0.2$, $D_u = 0.4$, $P_r = 1$.



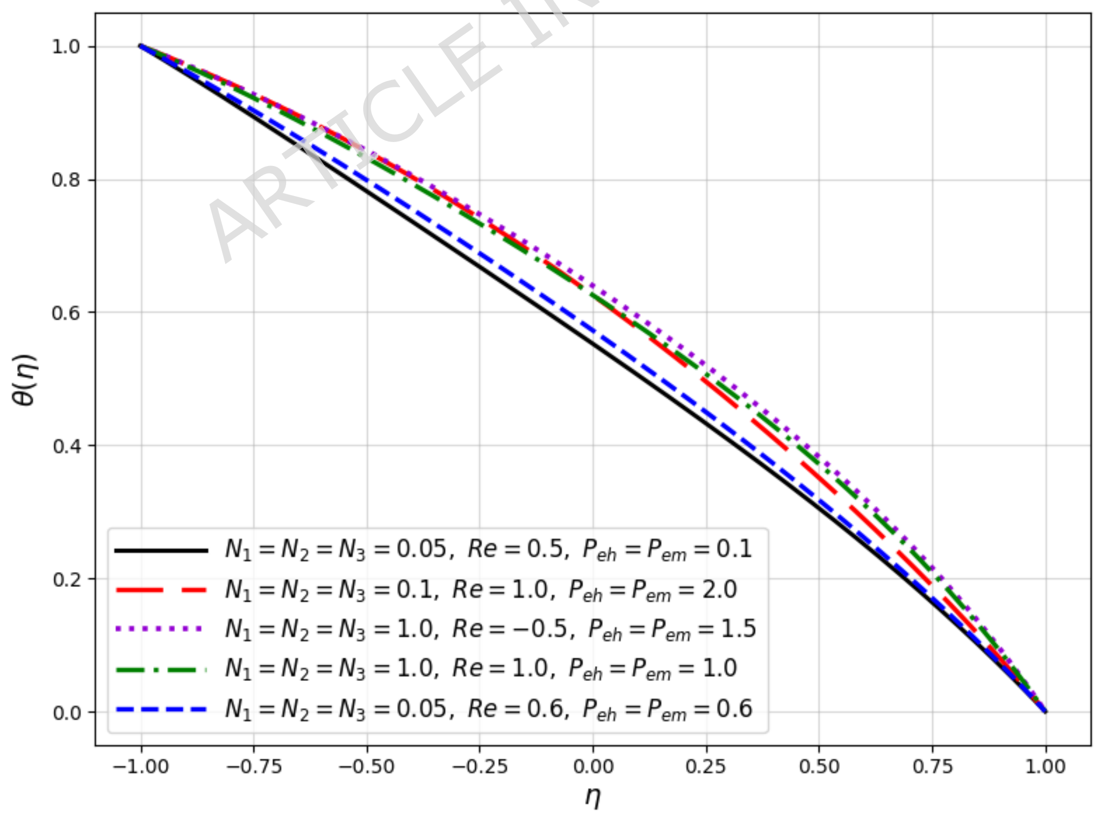


**Figure 7:** Effect of varying Reynolds number $Re$, material parameters $N_1$, $N_2$,$N_3$ and Peclet numbers $P_{eh}$,$P_{em}$ on the temperature distribution $\theta(\eta)$at $M = 0.5$, $Z = 1$, $d = 0.5$, $E_c = 0.2$, $R_d = 0.4$, $S_c = S_r = 0.2$, $D_u = 0.4$, $P_r = 1$.

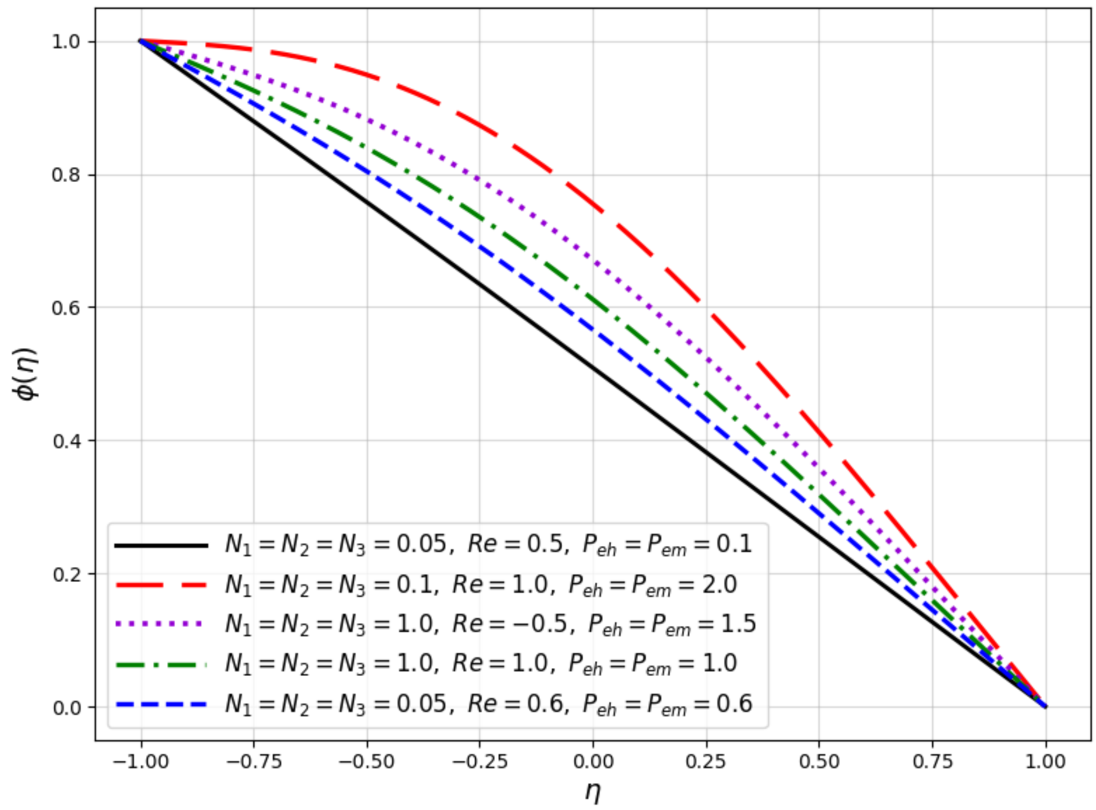


**Figure 8:** Effect of varying Reynolds number $Re$, material parameters $N_1$, $N_2$,$N_3$ and Peclet numbers $P_{eh}$,$P_{em}$ on the concentration distribution $\phi(\eta)$ at $M = 0.5$, $Z = 1$, $d = 0.5$, $E_c = 0.2$, $R_d = 0.4$, $S_c = S_r = 0.2$, $D_u = 0.4$, $P_r = 1$.



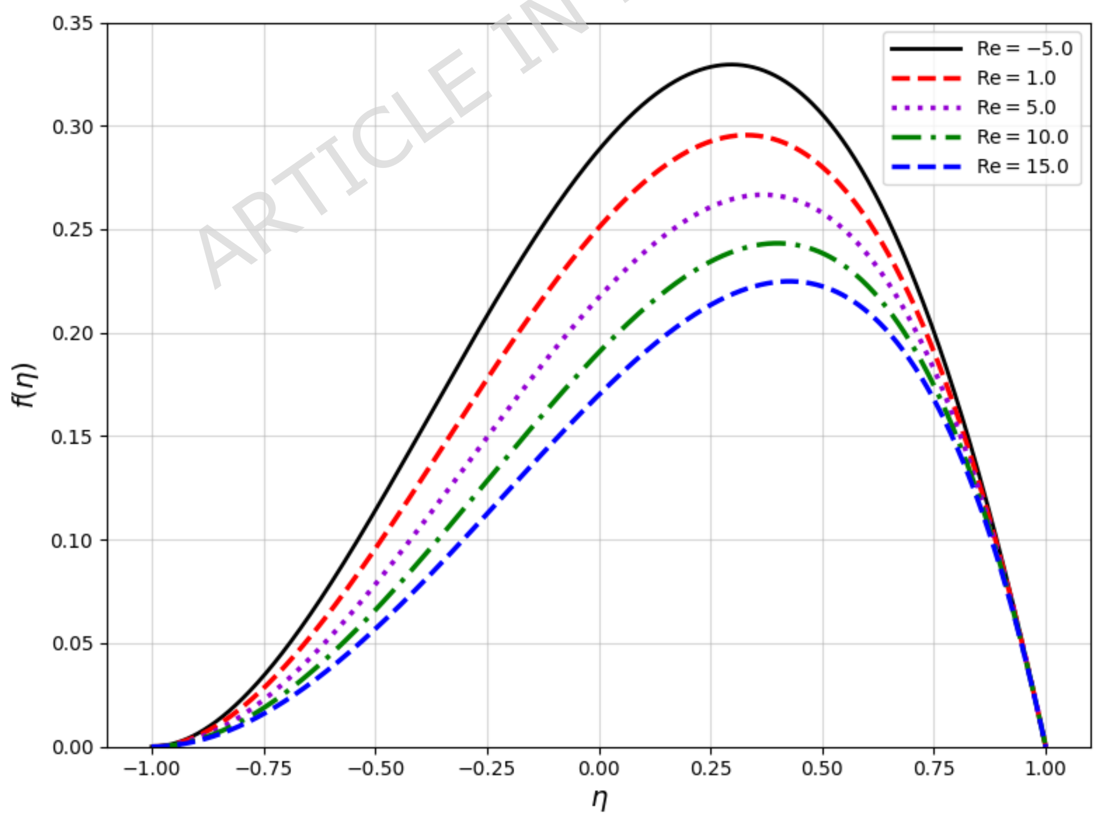


**Figure 9:** Effect of varying Reynolds number $Re$ on the stream function $f(\eta)$ at $N_1 = N_2 = N_3 = P_{eh} = P_{em} = 1$, $M = 0.5$, $Z = 1$, $d = 0.5$, $E_c = 0.2$, $R_d = 0.4$, $S_c = S_r = 0.2$, $D_u = 0.4$, $P_r = 1$.

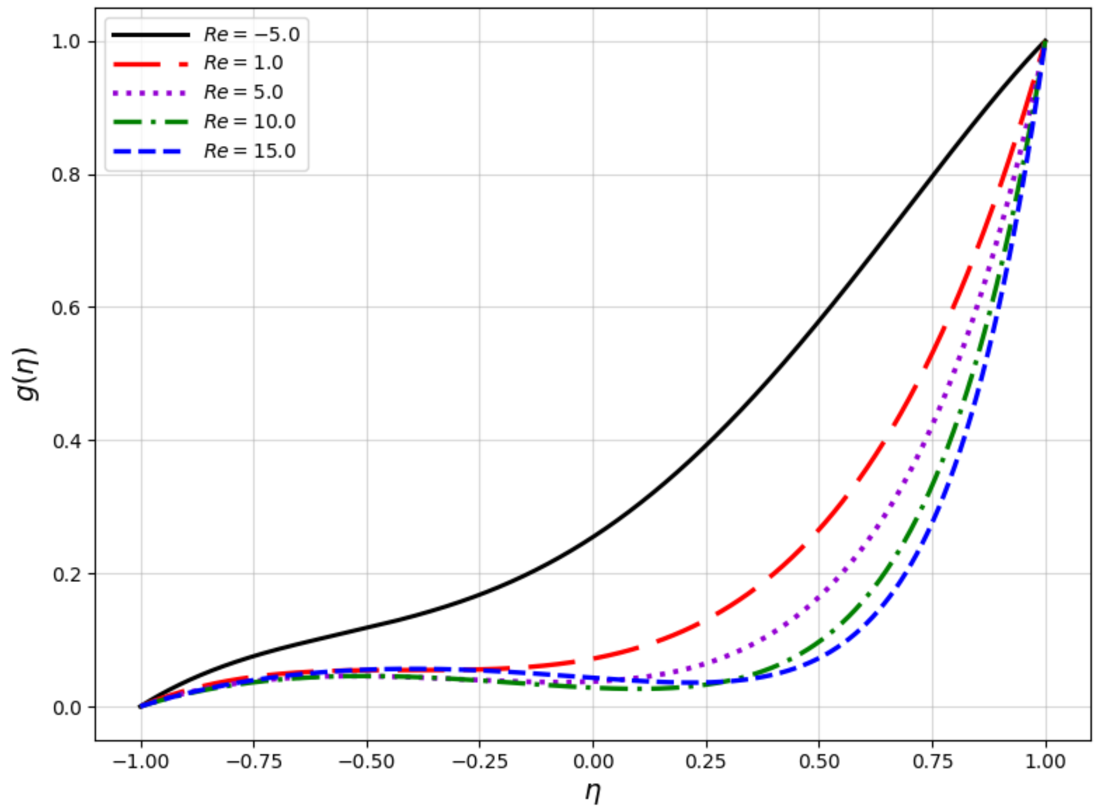


**Figure 10:** Effect of varying Reynolds number Re on the microrotation function $g(\eta)$ at $N_1 = N_2 = N_3 = P_{eh} = P_{em} = 1,\ M = 0.5,\ Z = 1,\ d = 0.5,\ E_c = 0.2,\ R_d = 0.4,\ S_c = S_r = 0.2,\ D_u = 0.4,\ P_r = 1.$



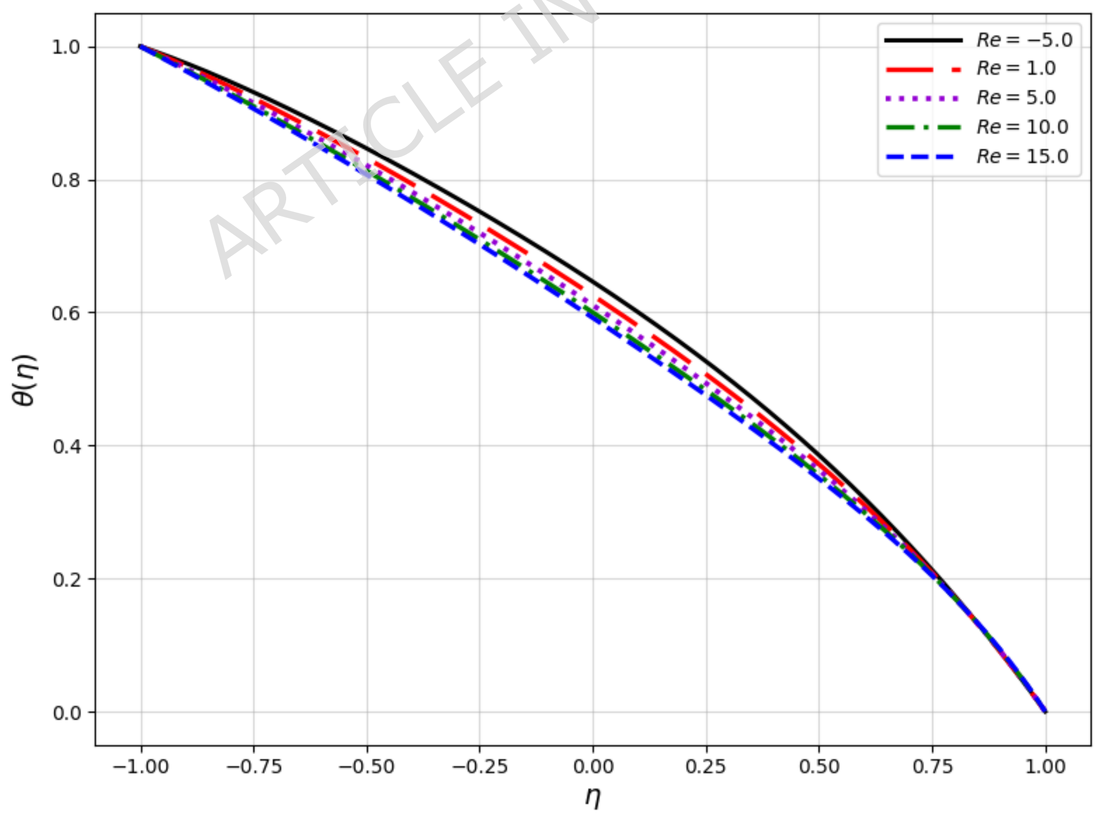


**Figure 11:** Effect of varying Reynolds number Re on the temperature distribution $\theta(\eta)$ at $N_1 = N_2 = N_3 = P_{eh} = P_{em} = 1,\ M = 0.5,\ Z = 1,\ d = 0.5,\ E_c = 0.2,\ R_d = 0.4,\ S_c = S_r = 0.2,\ D_u = 0.4,\ P_r = 1.$

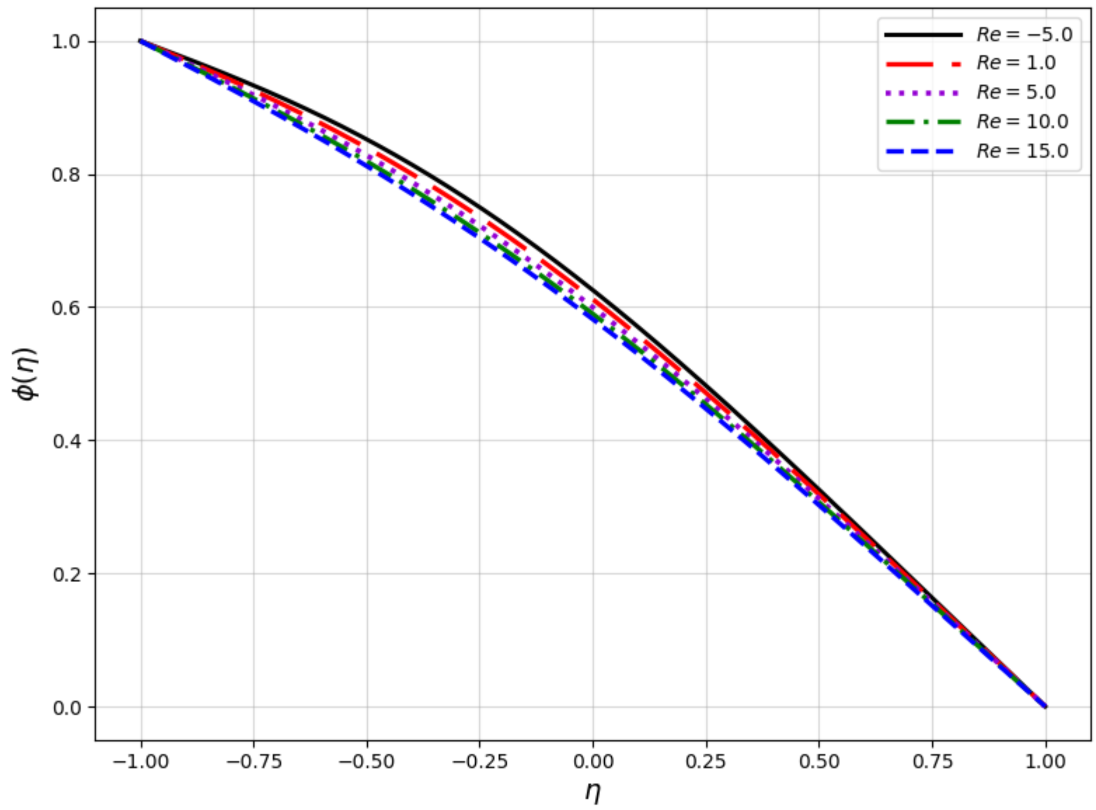


Figure 12: Effect of varying Reynolds number $Re$ on concentration distribution $\phi(\eta)$ at $N_1 = N_2 = N_3 = P_{eh} = P_{em} = 1$, $M = 0.5$, $Z = 1$, $d = 0.5$, $E_c = 0.2$, $R_d = 0.4$, $S_c = S_r = 0.2$, $D_u = 0.4$, $P_r = 1$.



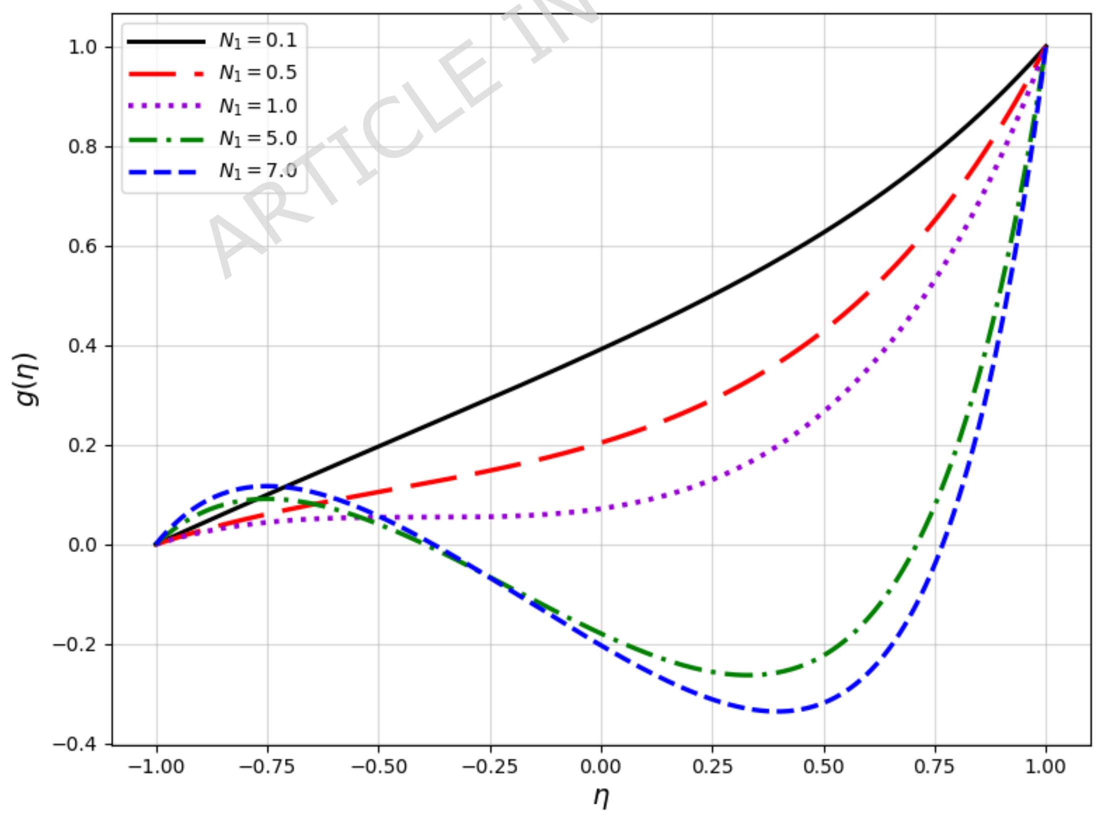


Figure 13: Effect of varying $N_1$ on the microrotation function $g(\eta)$ at $N_2 = N_3 = P_{eh} = P_{em} = 1$, $M = 0.5$, $Z = 1$, $d = 0.5$, $E_c = 0.2$, $R_e = 1$, $R_d = 0.4$, $S_c = S_r = 0.2$, $D_u = 0.4$, $P_r = 1$.

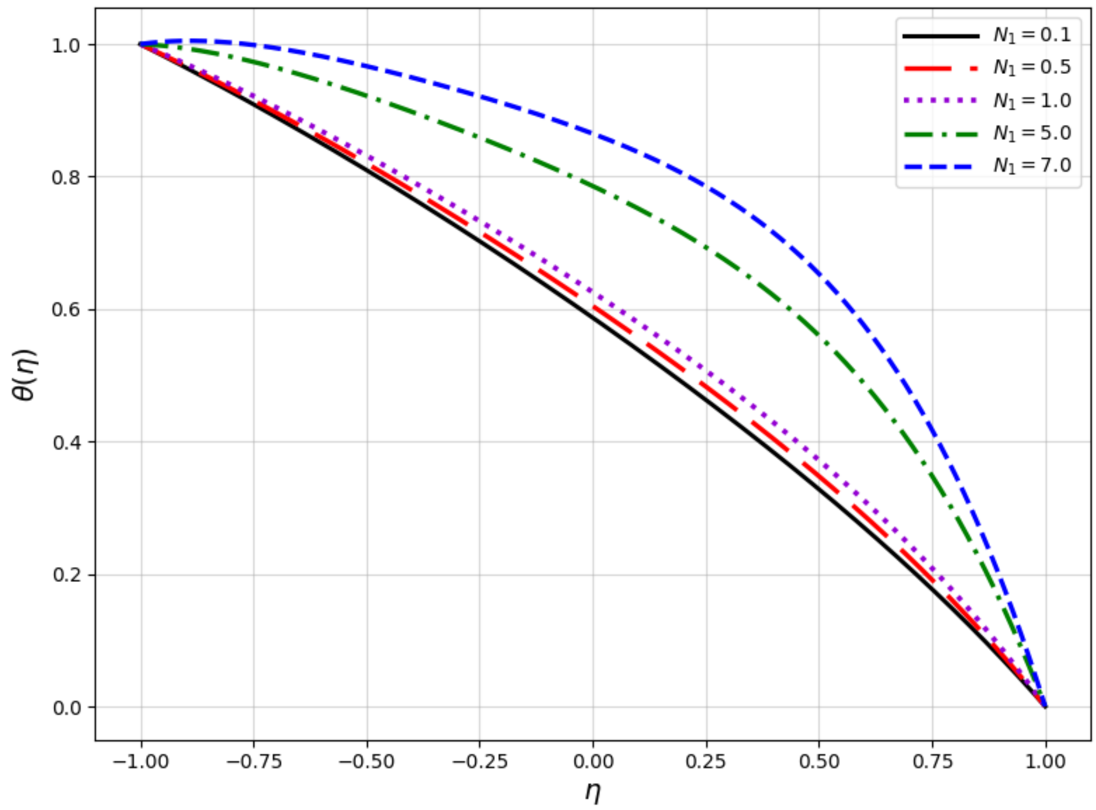


Figure 14: Effect of varying $N_1$ on the temperature distribution $\theta(\eta)$ at $N_2 = N_3 = P_{eh} = P_{em} = 1$, $M = 0.5$, $Z = 1$, $d = 0.5$, $E_c = 0.2$, $R_e = 1$, $R_d = 0.4$, $S_c = S_r = 0.2$, $D_u = 0.4$, $P_r = 1$.



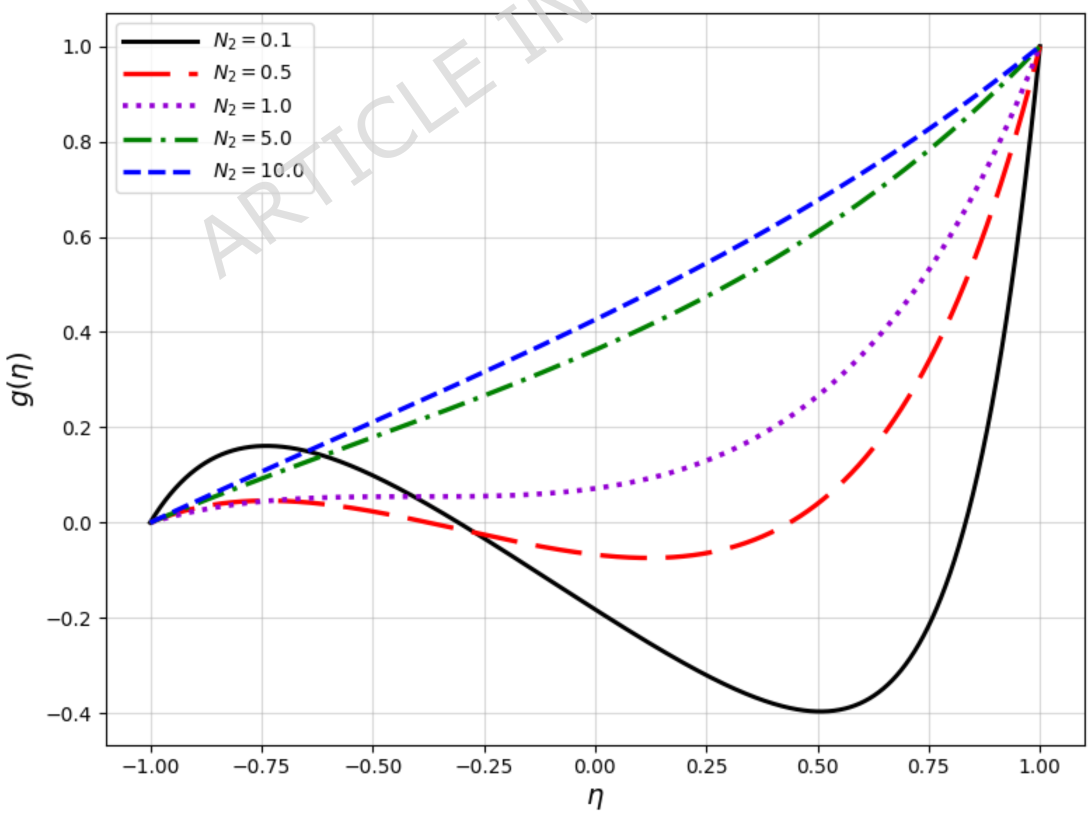


Figure 15: Effect of varying $N_2$ on the microrotation function $g(\eta)$ at $N_1 = N_3 = P_{eh} = P_{em} = 1$, $M = 0.5$, $Z = 1$, $d = 0.5$, $E_c = 0.2$, $R_e = 1$, $R_d = 0.4$, $S_c = S_r = 0.2$, $D_u = 0.4$, $P_r = 1$.

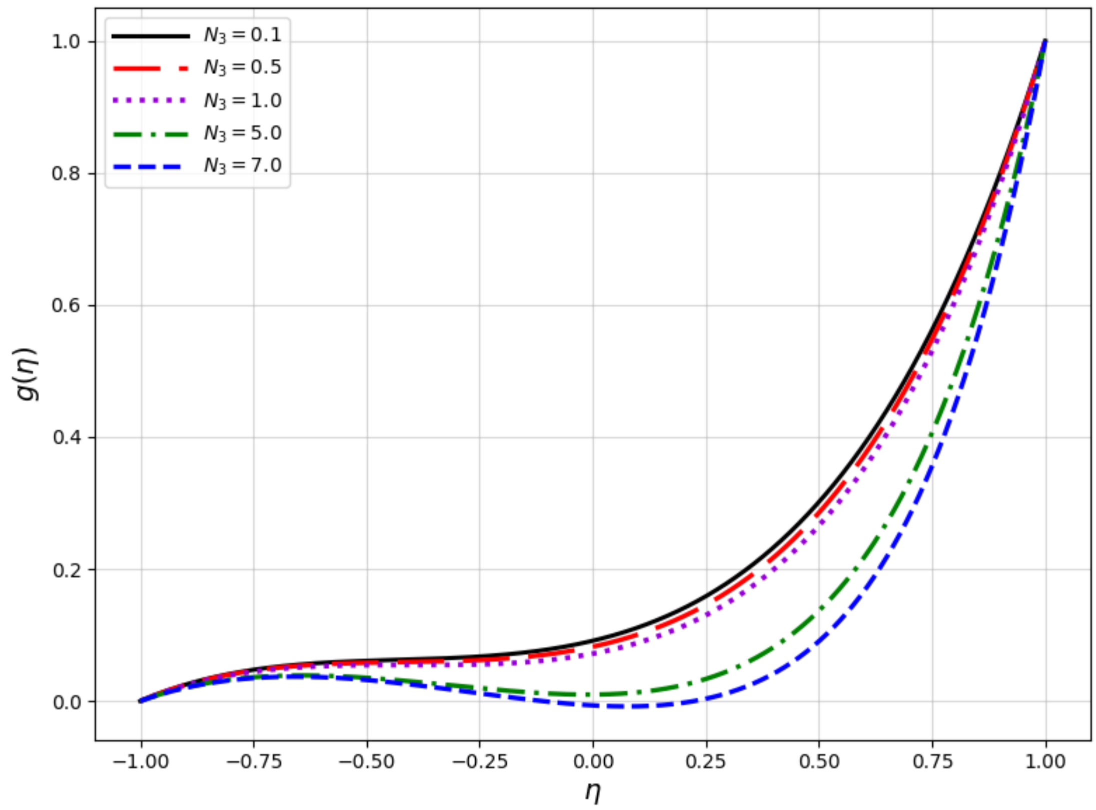


Figure 16: Effect of varying $N_3$ on the microrotation function $g(\eta)$ at $N_1 = N_2 = P_{eh} = P_{em} = 1$, $M = 0.5$, $Z = 1$, $d = 0.5$, $E_c = 0.2$, $R_e = 1$, $R_d = 0.4$, $S_c = S_r = 0.2$, $D_u = 0.4$, $P_r = 1$.



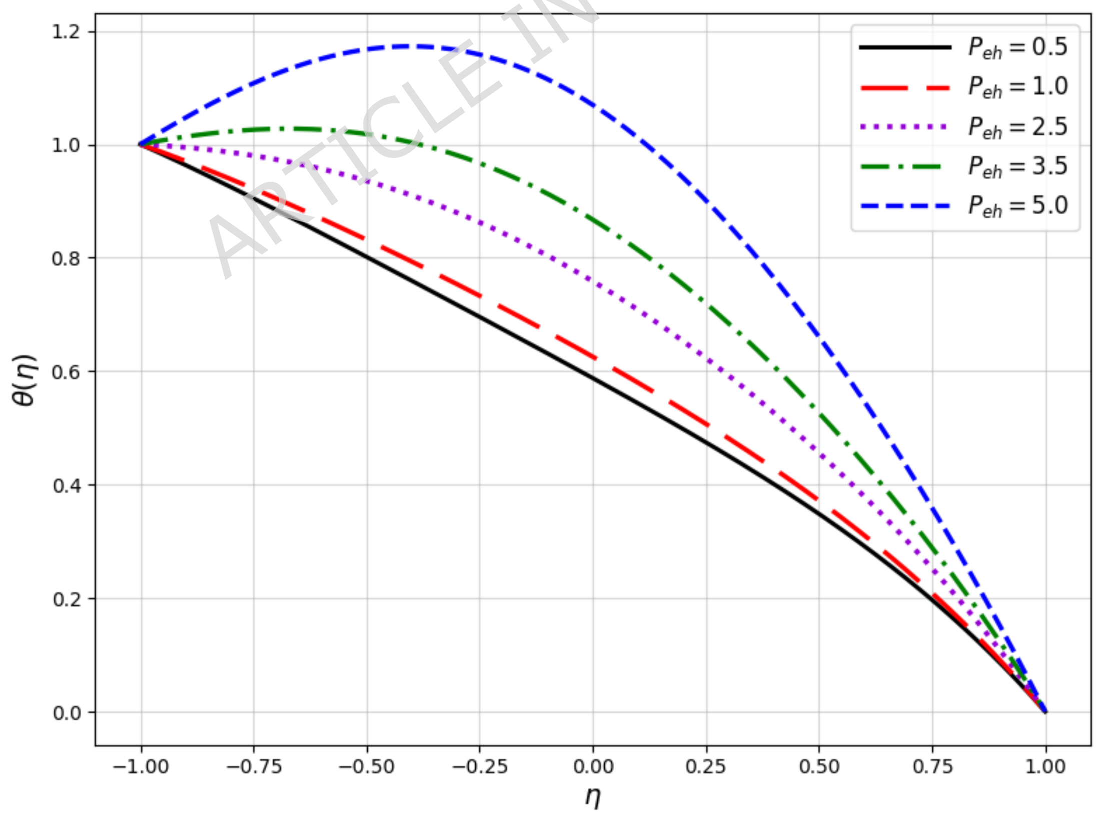


Figure 17: Effect of varying $P_{eh}$ on the temperature distribution $\theta(\eta)$ at $N_1 = N_2 = N_3 = P_{em} = 1$, $M = 0.5$, $Z = 1$, $d = 0.5$, $E_c = 0.2$, $R_e = 1$, $R_d = 0.4$, $S_c = S_r = 0.2$, $D_u = 0.4$, $P_r = 1$.

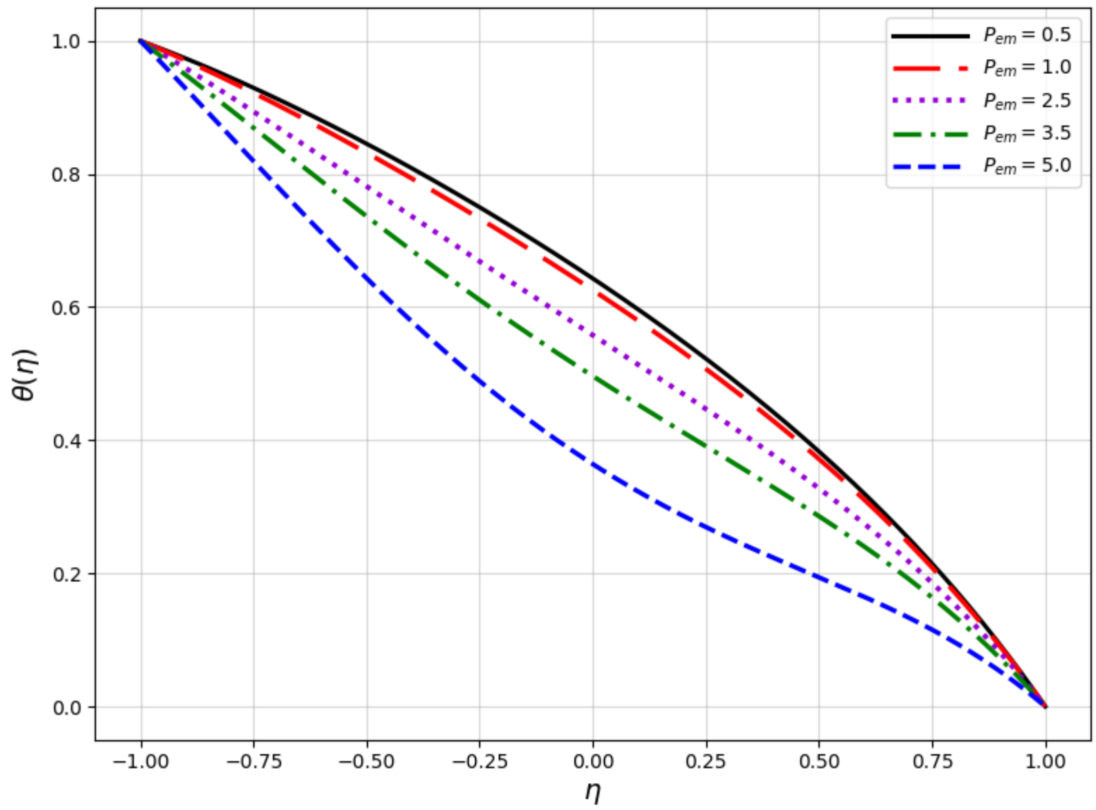


Figure 18: Effect of varying $P_{em}$ on the temperature distribution $\theta(\eta)$ at $N_1 = N_2 = N_3 = P_{eh} = 1$, $M = 0.5$, $Z = 1$, $d = 0.5$, $E_c = 0.2$, $R_e = 1$, $R_d = 0.4$, $S_c = S_r = 0.2$, $D_u = 0.4$, $P_r = 1$.



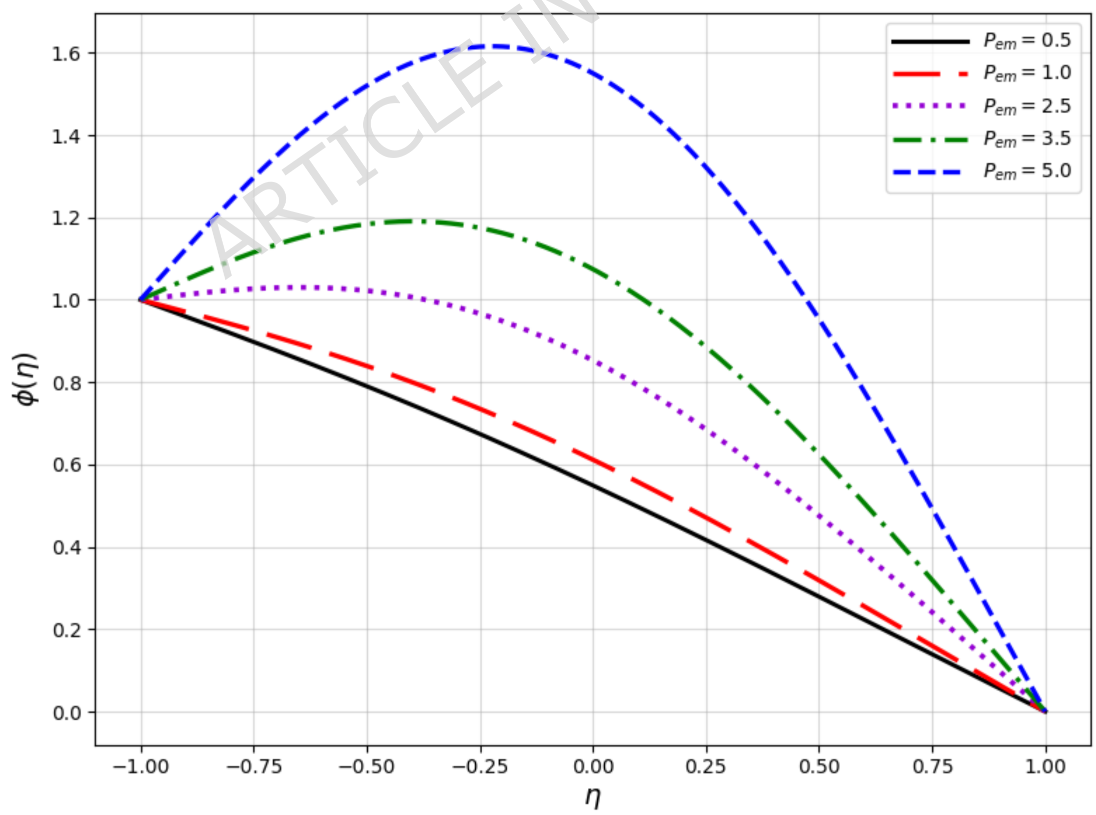


Figure 19: Effect of varying $P_{em}$ on the concentration distribution $\phi(\eta)$ at $N_1 = N_2 = N_3 = P_{eh} = 1$, $M = 0.5$, $Z = 1$, $d = 0.5$, $E_c = 0.2$, $R_e = 1$, $R_d = 0.4$, $S_c = S_r = 0.2$, $D_u = 0.4$, $P_r = 1$.

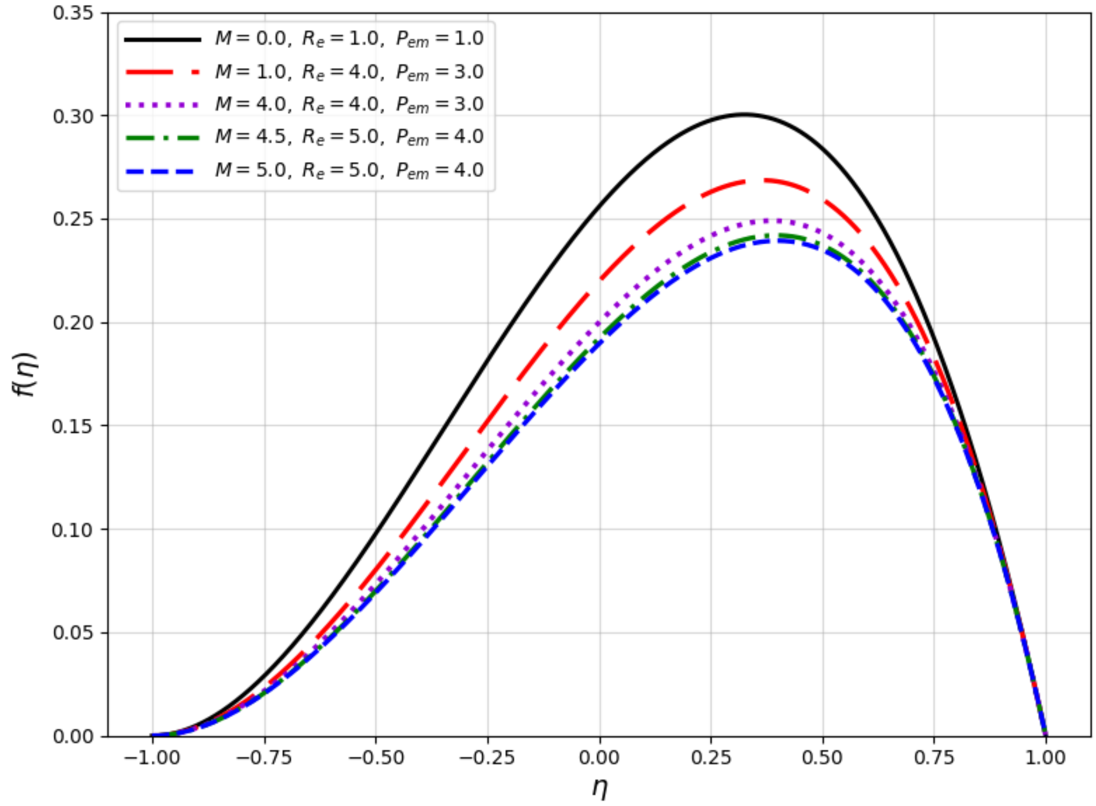


Figure 20: Effect of varying M, $R_e$ and $P_{em}$ on the stream function $f(\eta)$ at $N_1 = N_2 = N_3 = P_{eh} = 1$, $Z = 1$, $d = 0.5$, $E_c = 0.2$, $R_d = 0.4$, $S_c = S_r = 0.2$, $D_u = 0.4$, $P_r = 1$.

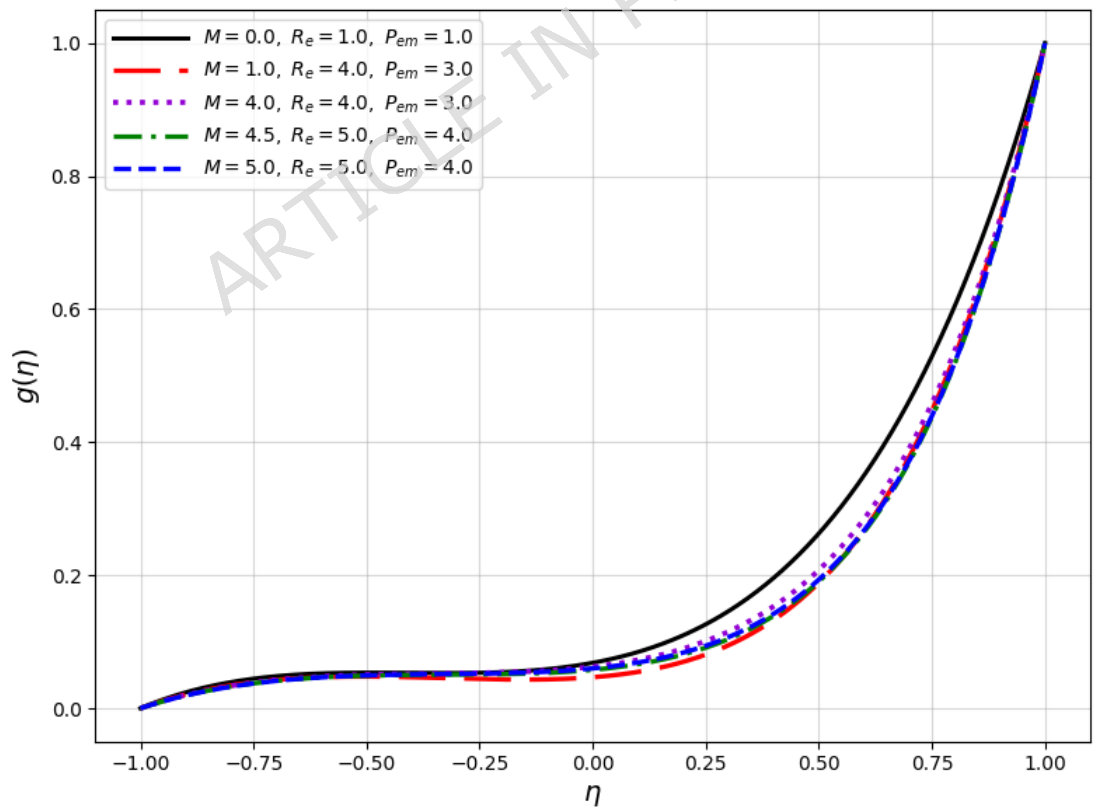


Figure 21: Effect of varying M, $R_e$ and $P_{em}$ on the microrotation function $g(\eta)$ at $N_1 = N_2 = N_3 = P_{eh} = 1$, $Z = 1$, $d = 0.5$, $E_c = 0.2$, $R_d = 0.4$, $S_c = S_r = 0.2$, $D_u = 0.4$, $P_r = 1$.

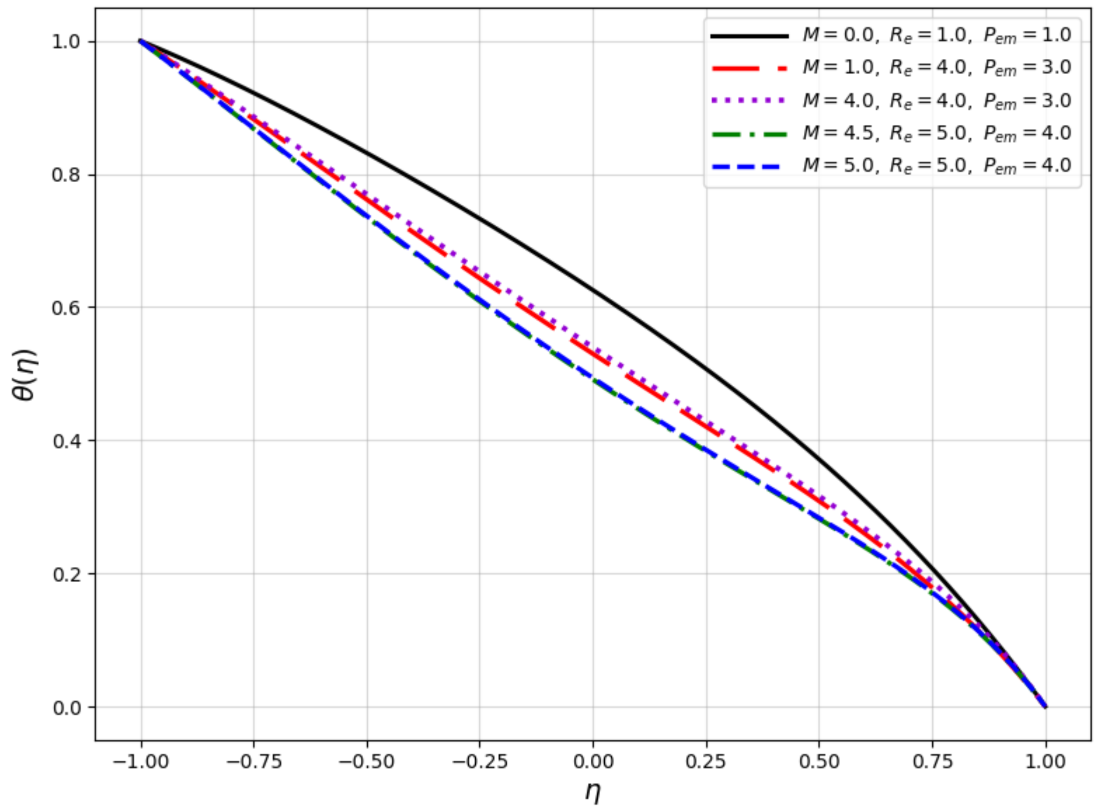


Figure 22: Effect of varying $M$, $R_e$ and $P_{em}$ on the temperature distribution $\theta(\eta)$ at $N_1 = N_2 = N_3 = P_{eh} = 1$, $Z = 1$, $d = 0.5$, $E_c = 0.2$, $R_d = 0.4$, $S_c = S_r = 0.2$, $D_u = 0.4$, $P_r = 1$.



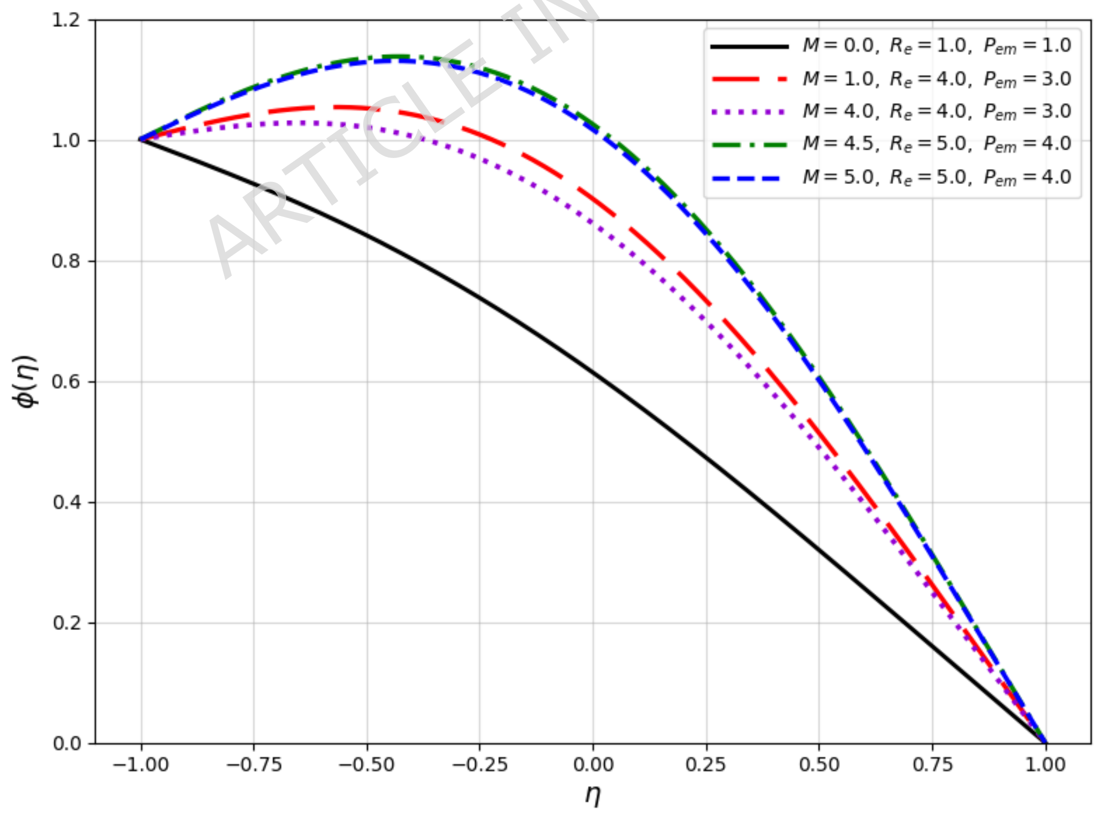


Figure 23: Effect of varying $M$, $R_e$ and $P_{em}$ on the concentration distribution $\phi(\eta)$ at $N_1 = N_2 = N_3 = P_{eh} = 1$, $Z = 1$, $d = 0.5$, $E_c = 0.2$, $R_d = 0.4$, $S_c = S_r = 0.2$, $D_u = 0.4$, $P_r = 1$.

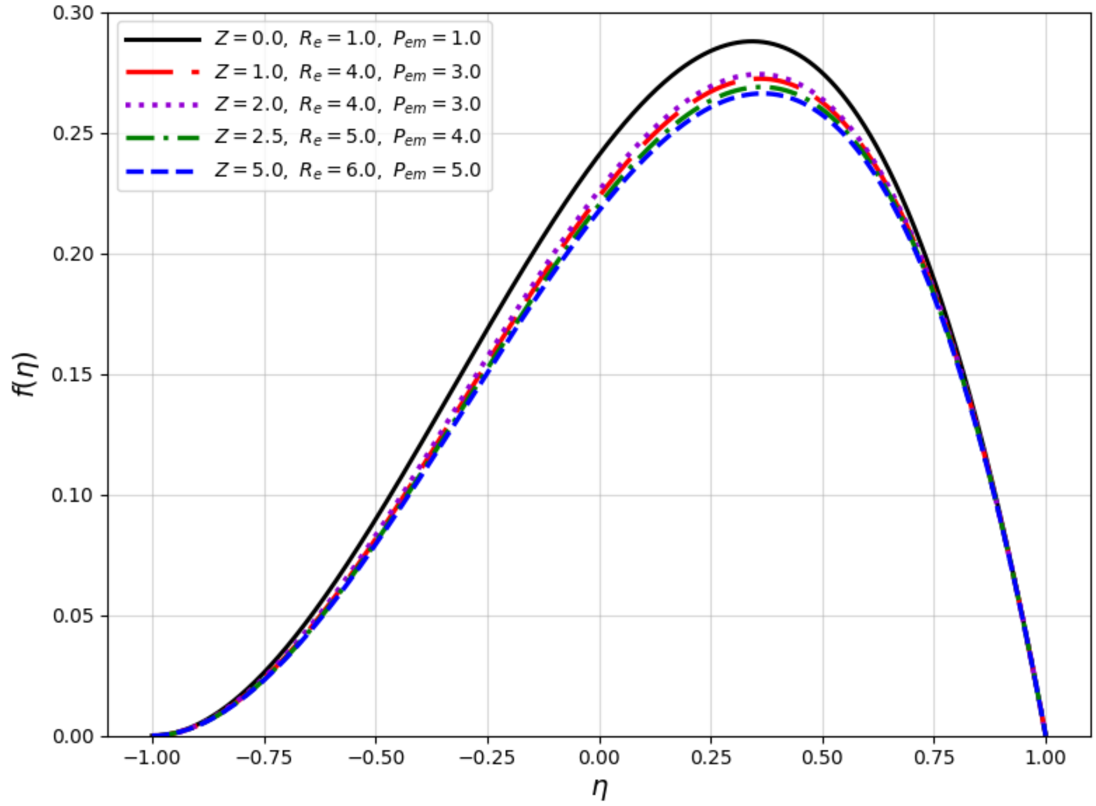


Figure 24: Effect of varying $Z$, $R_e$ and $P_{em}$ on the stream function $f(\eta)$ at $N_1 = N_2 = N_3 = P_{eh} = 1$, $M = 0.5$, $d = 0.5$, $E_c = 0.2$, $R_d = 0.4$, $S_c = S_r = 0.2$, $D_u = 0.4$, $P_r = 1$.



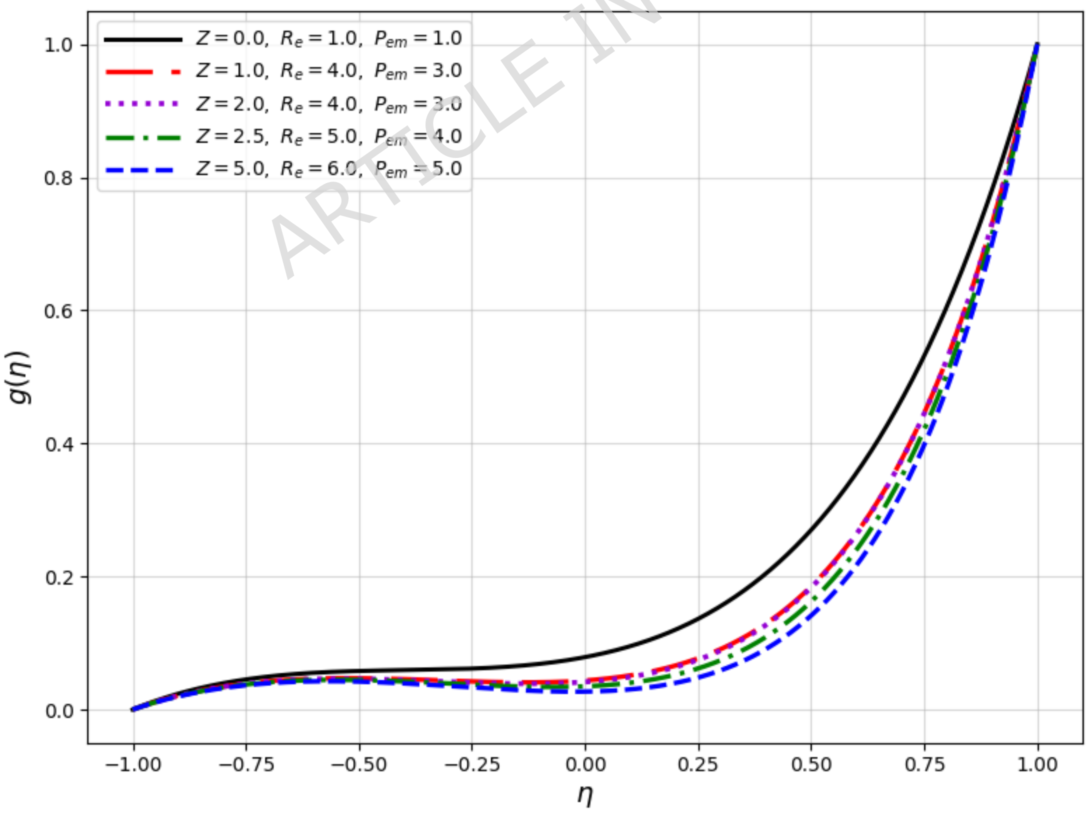


Figure 25: Effect of varying $Z$, $R_e$ and $P_{em}$ on the microrotation function $g(\eta)$ at $N_1 = N_2 = N_3 = P_{eh} = 1$, $M = 0.5$, $d = 0.5$, $E_c = 0.2$, $R_d = 0.4$, $S_c = S_r = 0.2$, $D_u = 0.4$, $P_r = 1$.

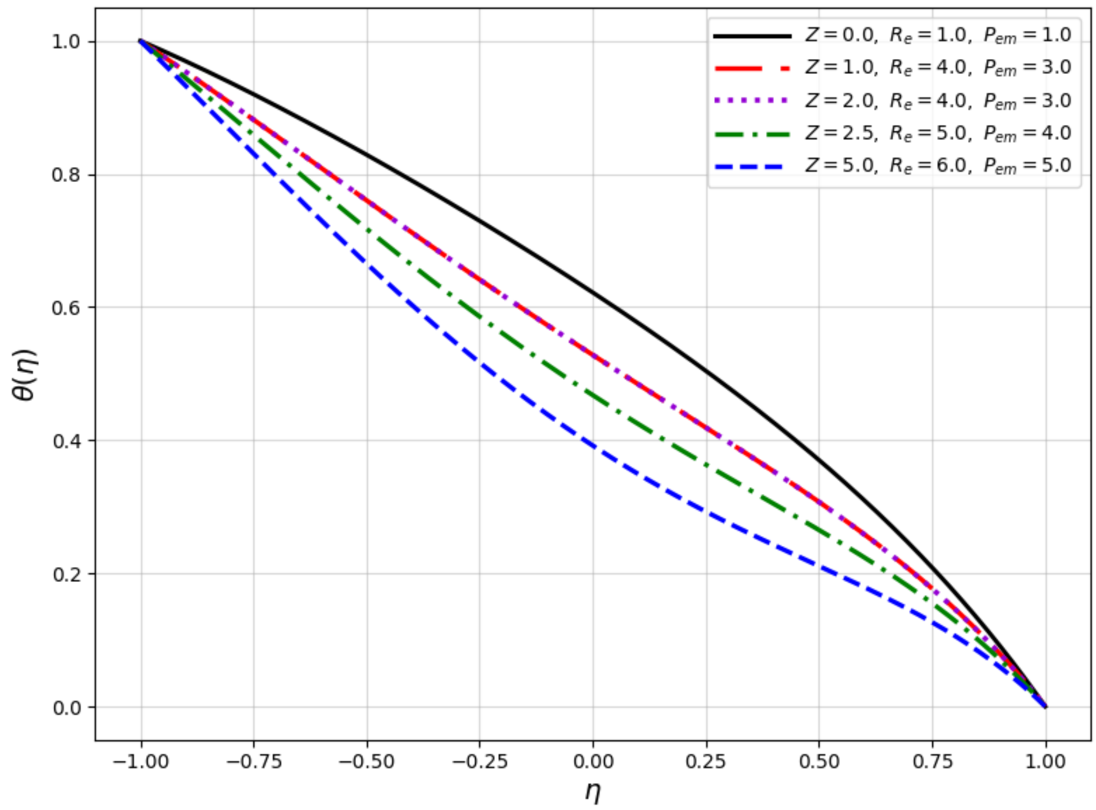


Figure 26: Effect of varying Z, $R_e$ and $P_{em}$ on the temperature distribution $\theta(\eta)$ at $N_1 = N_2 = N_3 = P_{eh} = 1$, $M = 0.5$, $d = 0.5$, $E_c = 0.2$, $R_d = 0.4$, $S_c = S_r = 0.2$, $D_u = 0.4$, $P_r = 1$.

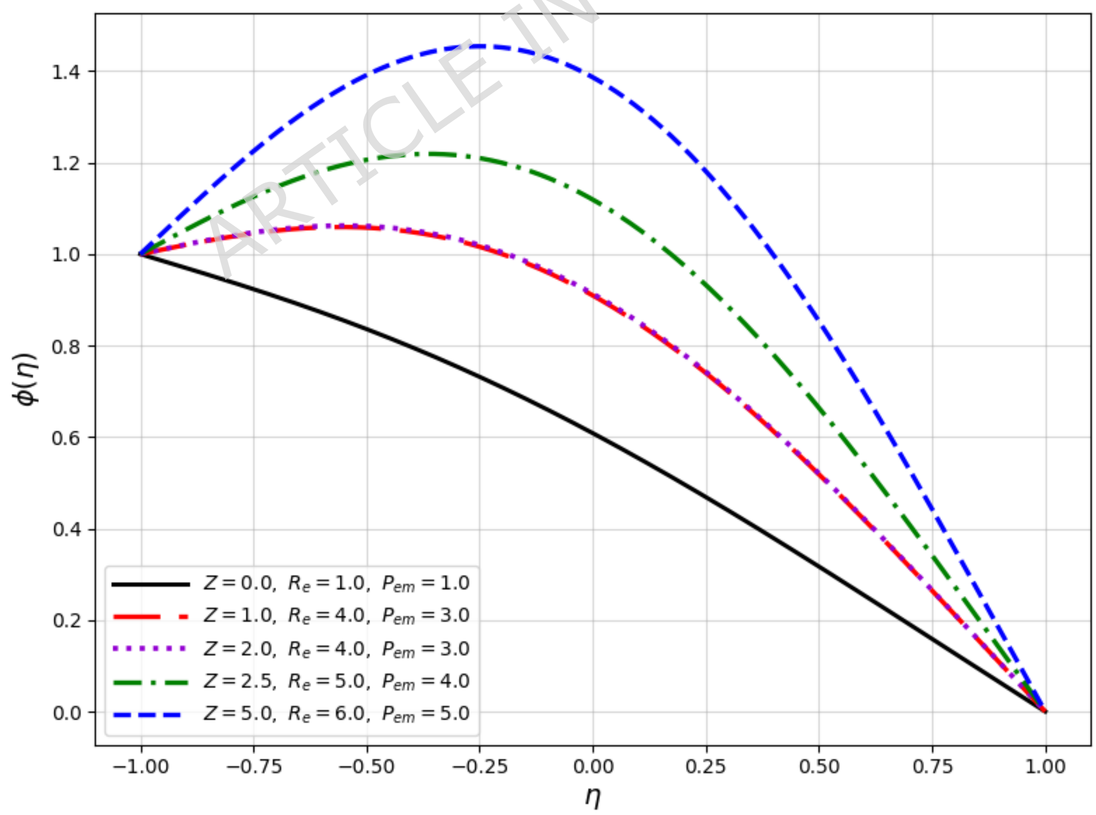


Figure 27: Effect of varying Z, $R_e$ and $P_{em}$ on the concentration distribution $\phi(\eta)$ at $N_1 = N_2 = N_3 = P_{eh} = 1$, $M = 0.5$, $d = 0.5$, $E_c = 0.2$, $R_d = 0.4$, $S_c = S_r = 0.2$, $D_u = 0.4$, $P_r = 1$.

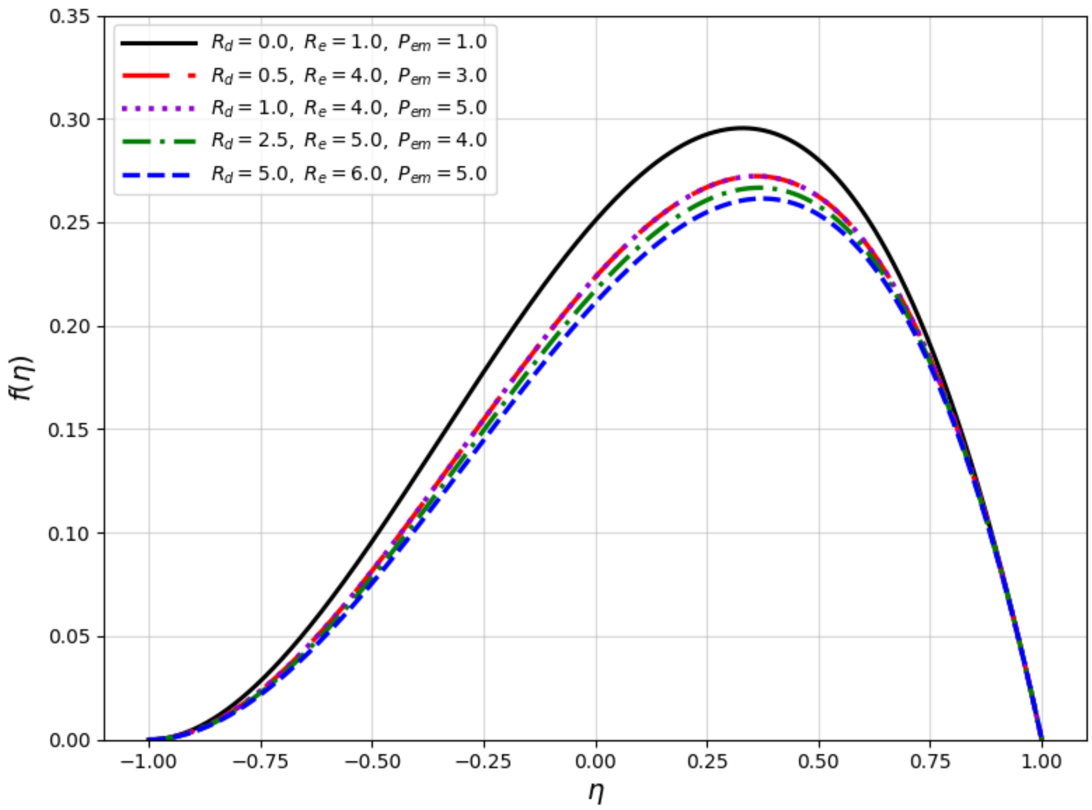


Figure 28: Effect of varying $R_d$, $R_e$ and $P_{em}$ on the stream function $f(\eta)$ at $N_1 = N_2 = N_3 = P_{eh} = Z = 1$, $M = 0.5$, $d = 0.5$, $E_c = 0.2$, $S_c = S_r = 0.2$, $D_u = 0.4$, $P_r = 1$.



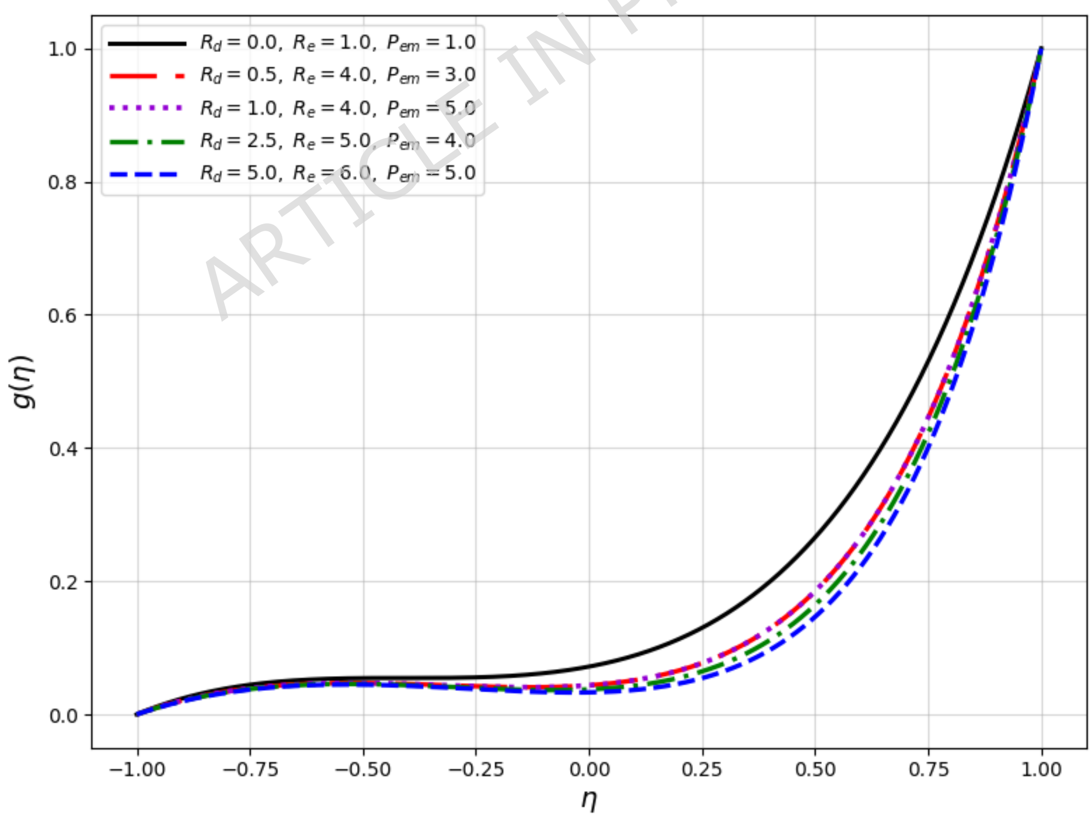


Figure 29: Effect of varying $R_d$, $R_e$ and $P_{em}$ on the microrotation function $g(\eta)$ at $N_1 = N_2 = N_3 = P_{eh} = Z = 1$, $M = 0.5$, $d = 0.5$, $E_c = 0.2$, $S_c = S_r = 0.2$, $D_u = 0.4$, $P_r = 1$.

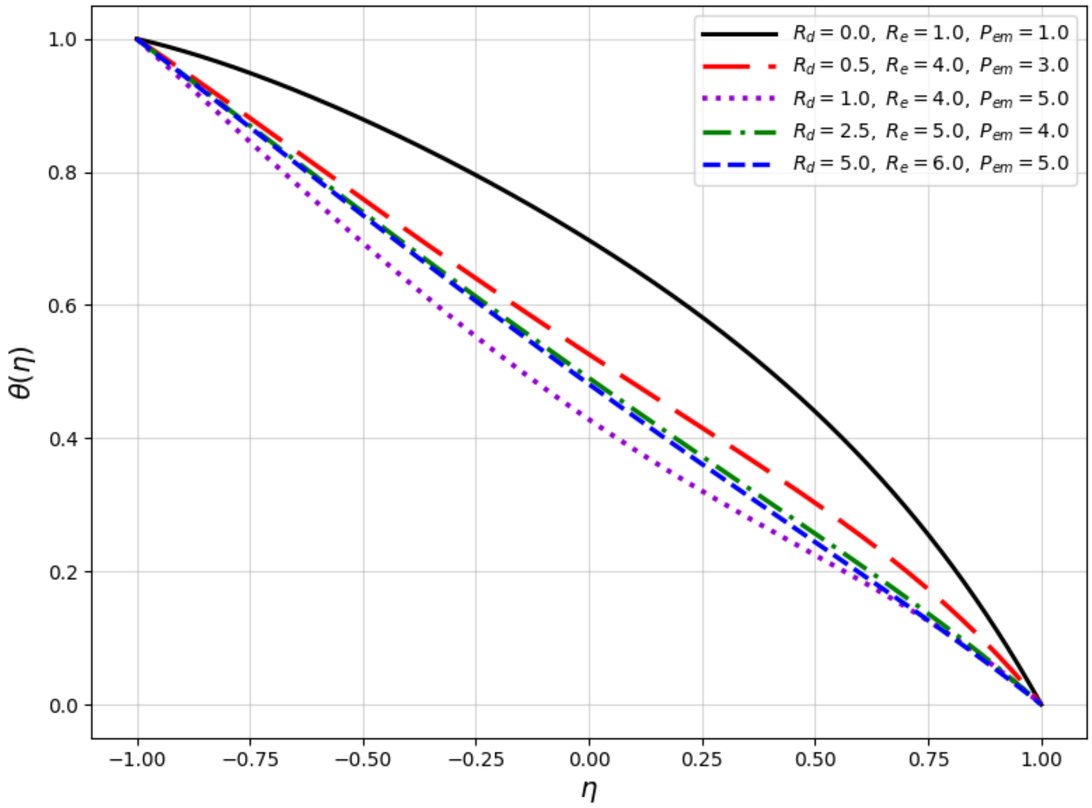


Figure 30: Effect of varying $R_d$, $R_e$ and $P_{em}$ on the temperature distribution $\theta(\eta)$ at $N_1 = N_2 = N_3 = P_{eh} = Z = 1$, $M = 0.5$, $d = 0.5$, $E_c = 0.2$, $S_c = S_r = 0.2$, $D_u = 0.4$, $P_r = 1$.



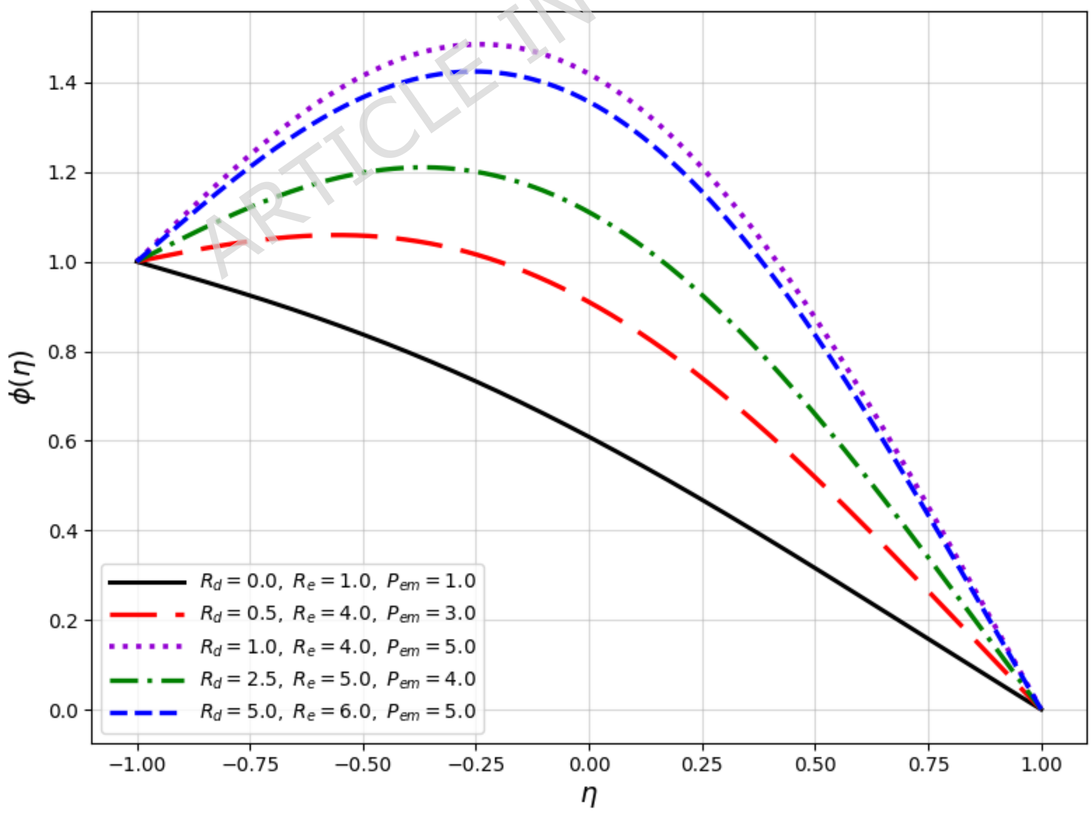


Figure 31: Effect of varying $R_d$, $R_e$ and $P_{em}$ on the concentration distribution $\phi(\eta)$ at $N_1 = N_2 = N_3 = P_{eh} = Z = 1$, $M = 0.5$, $d = 0.5$, $E_c = 0.2$, $S_c = S_r = 0.2$, $D_u = 0.4$, $P_r = 1$.

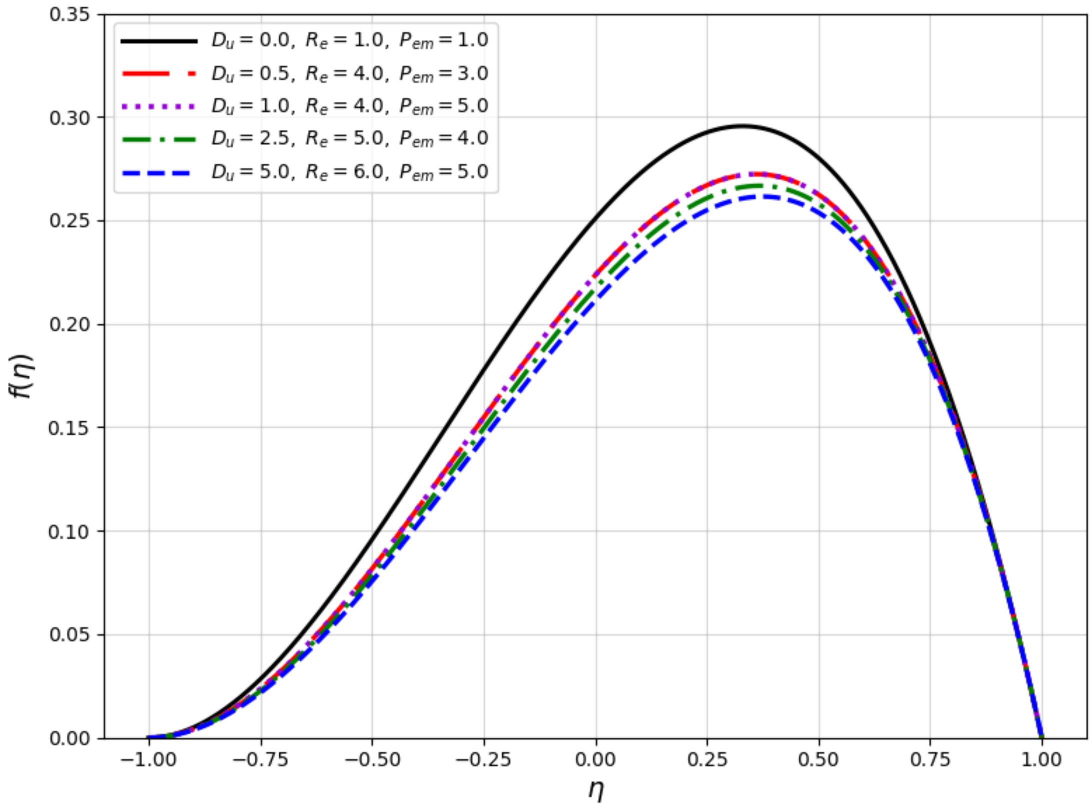


Figure 32: Effect of varying $D_u$, $R_e$ and $P_{em}$ on the stream function $f(\eta)$ at $N_1 = N_2 = N_3 = P_{eh} = Z = 1$, $M = 0.5$, $d = 0.5$, $R_d = 0.4$, $E_c = 0.2$, $S_c = S_r = 0.2$, $P_r = 1$.



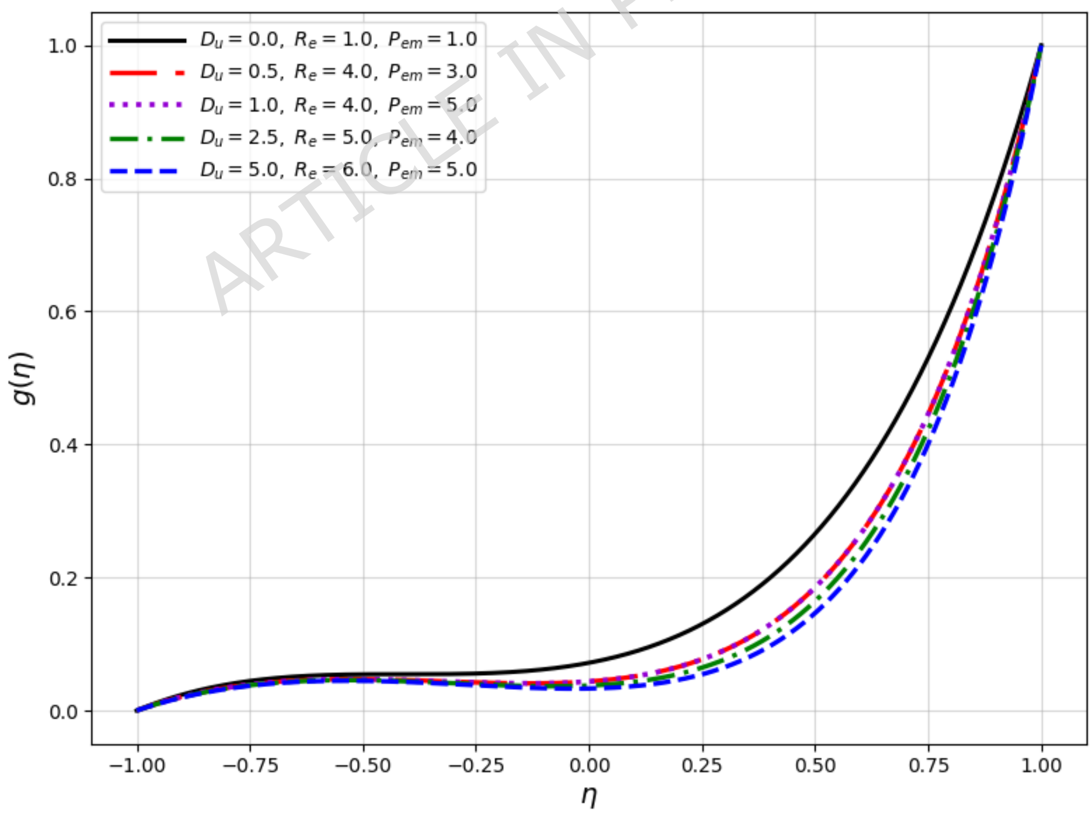


Figure 33: Effect of varying $D_u$, $R_e$ and $P_{em}$ on the microrotation function $g(\eta)$ at $N_1 = N_2 = N_3 = P_{eh} = Z = 1$, $M = 0.5$, $d = 0.5$, $R_d = 0.4$, $E_c = 0.2$, $S_c = S_r = 0.2$, $P_r = 1$.

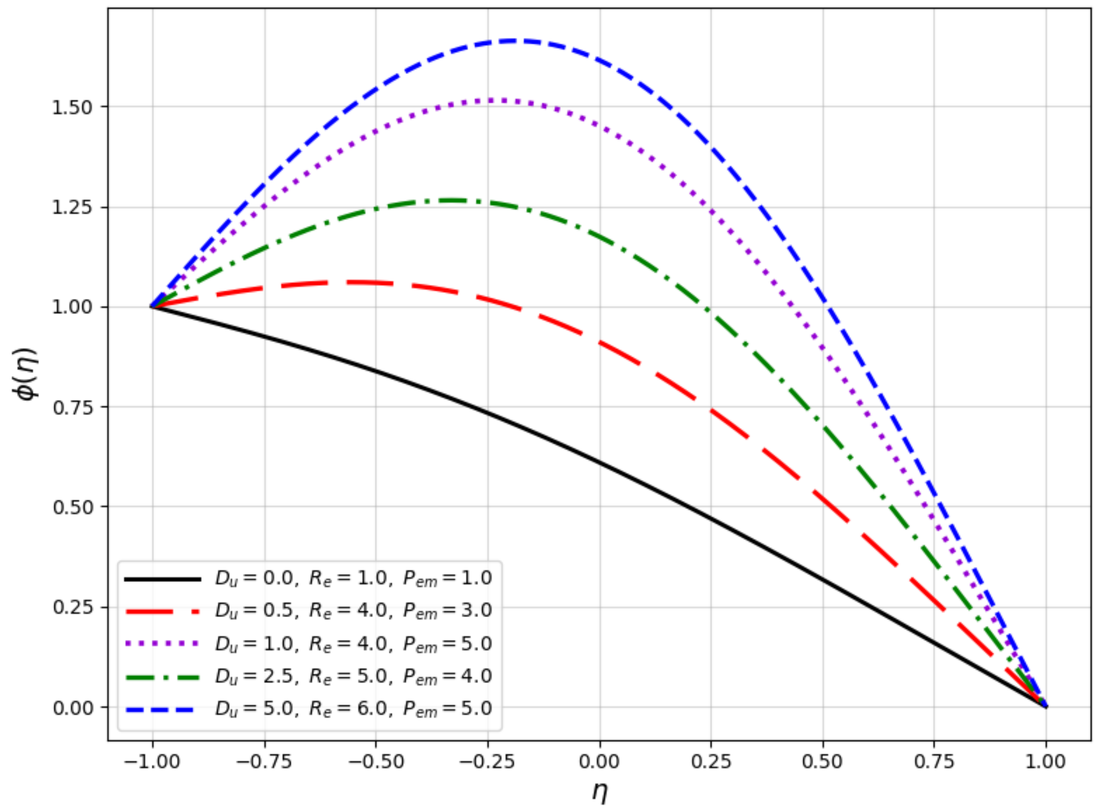


Figure 34: Effect of varying $D_u$, $R_e$ and $P_{em}$ on the concentration distribution $\phi(\eta)$ at $N_1 = N_2 = N_3 = P_{eh} = Z = 1$, $M = 0.5$, $d = 0.5$, $R_d = 0.4$, $E_c = 0.2$, $S_c = S_r = 0.2$, $P_r = 1$.



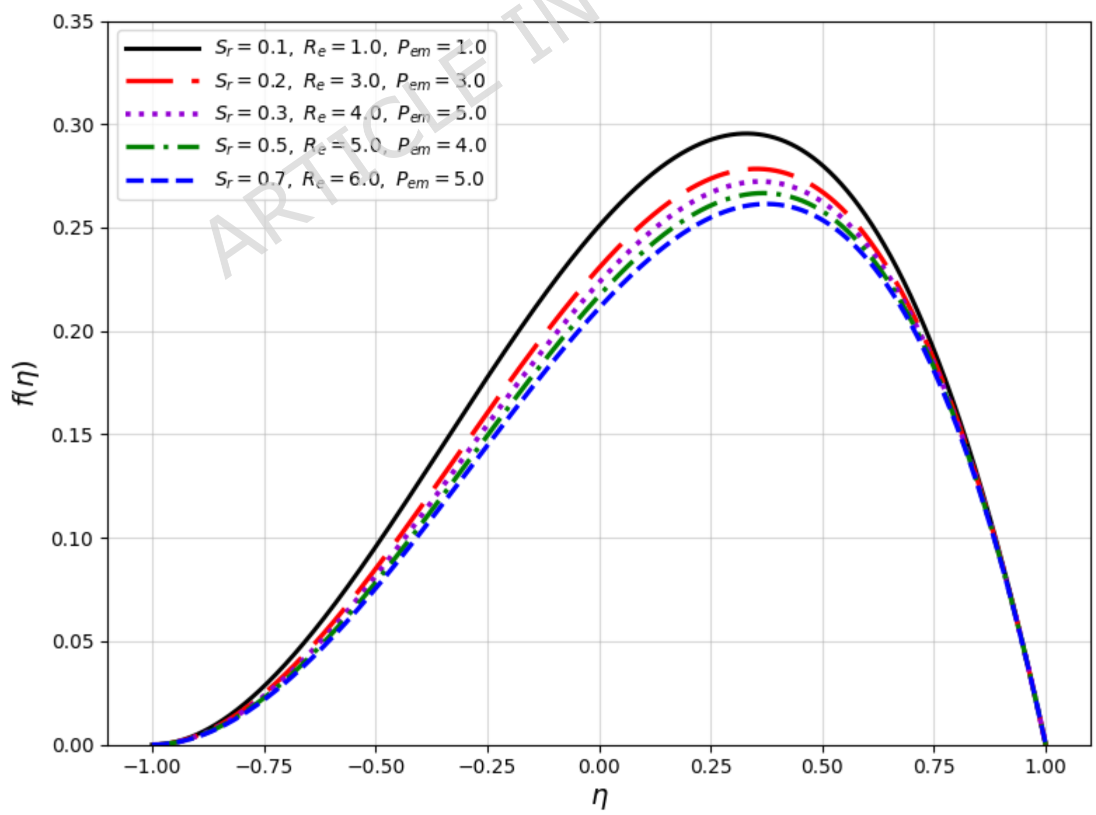


Figure 35: Effect of varying $S_r$, $R_e$ and $P_{em}$ on the stream function $f(\eta)$ at $N_1 = N_2 = N_3 = P_{eh} = Z = 1$, $M = 0.5$, $d = 0.5$, $R_d = 0.4$, $E_c = 0.2$, $S_c = 0.2$, $D_u = 0.4$, $P_r = 1$.

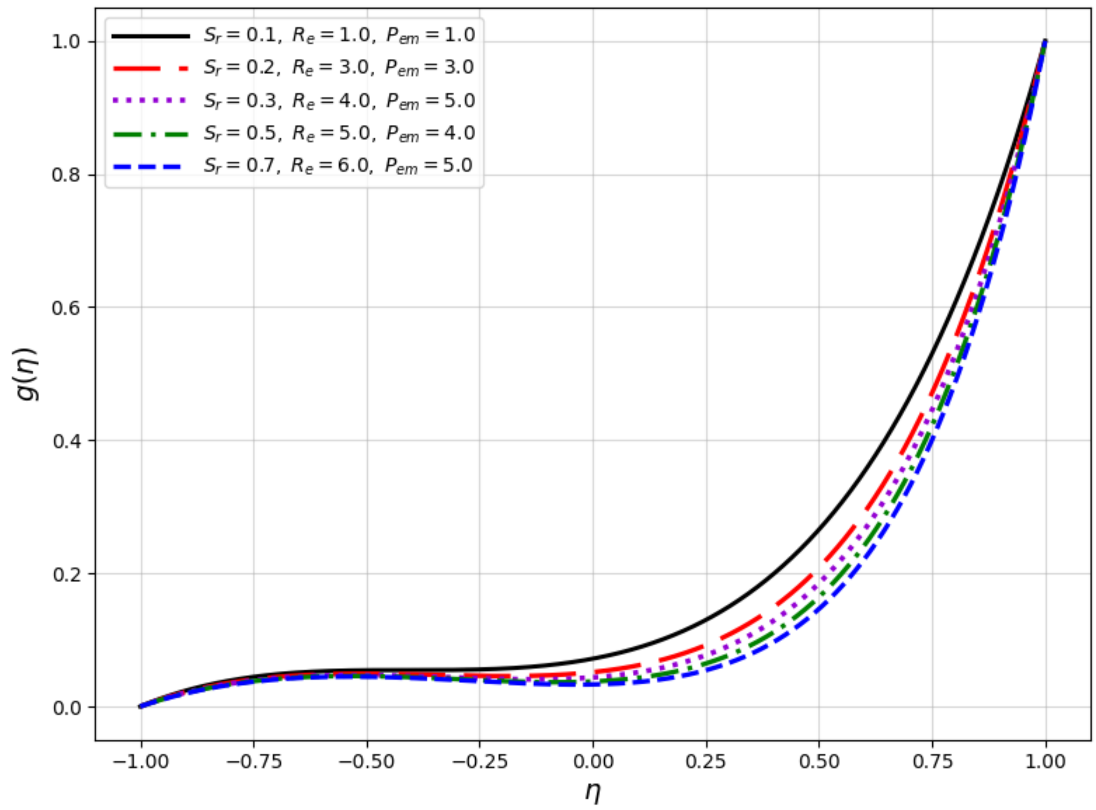


Figure 36: Effect of varying $S_r$, $R_e$ and $P_{em}$ on the microrotation function $g(\eta)$ at $N_1 = N_2 = N_3 = P_{eh} = Z = 1$, $M = 0.5$, $d = 0.5$, $R_d = 0.4$, $E_c = 0.2$, $S_c = 0.2$, $D_u = 0.4$, $P_r = 1$.



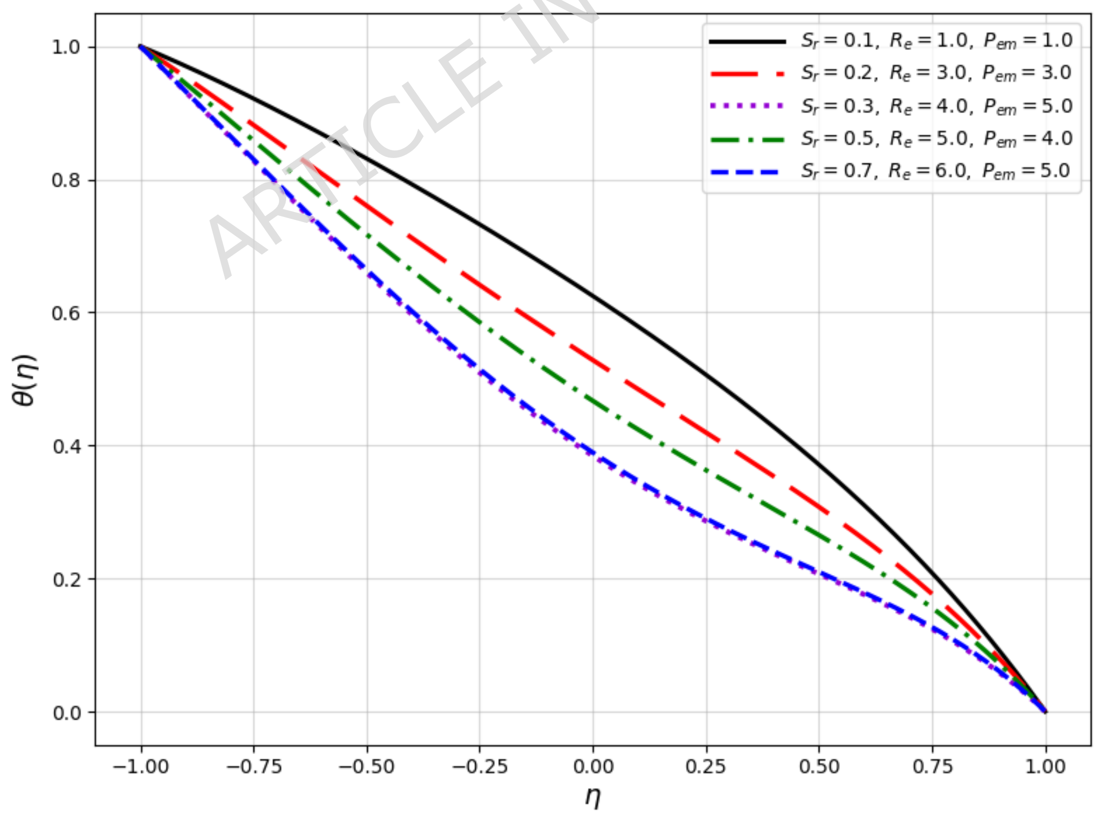


Figure 37: Effect of varying $S_r$, $R_e$ and $P_{em}$ on the temperature distribution $\theta(\eta)$ at $N_1 = N_2 = N_3 = P_{eh} = Z = 1$, $M = 0.5$, $d = 0.5$, $R_d = 0.4$, $E_c = 0.2$, $S_c = 0.2$, $D_u = 0.4$, $P_r = 1$.

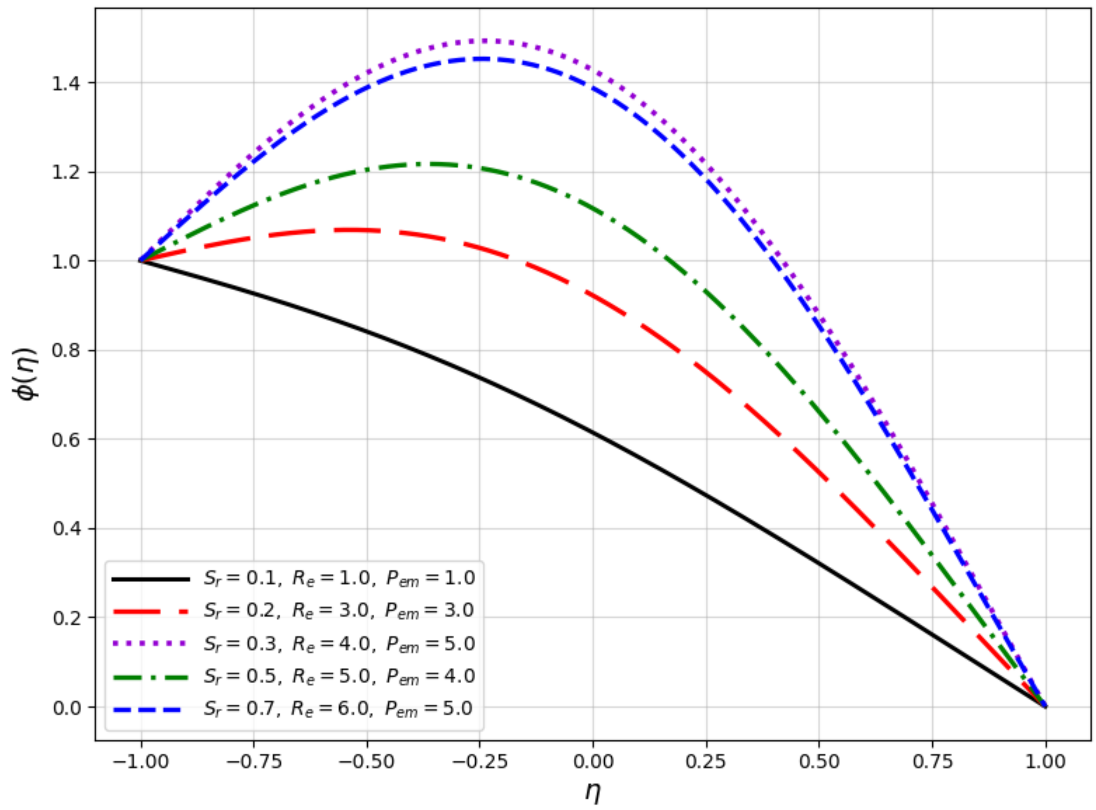


Figure 38: Effect of varying $S_r$, $R_e$ and $P_{em}$ on the concentration distribution $\phi(\eta)$ at $N_1 = N_2 = N_3 = P_{eh} = Z = 1$, $M = 0.5$, $d = 0.5$, $R_d = 0.4$, $E_c = 0.2$, $S_c = 0.2$, $D_u = 0.4$, $P_r = 1$.



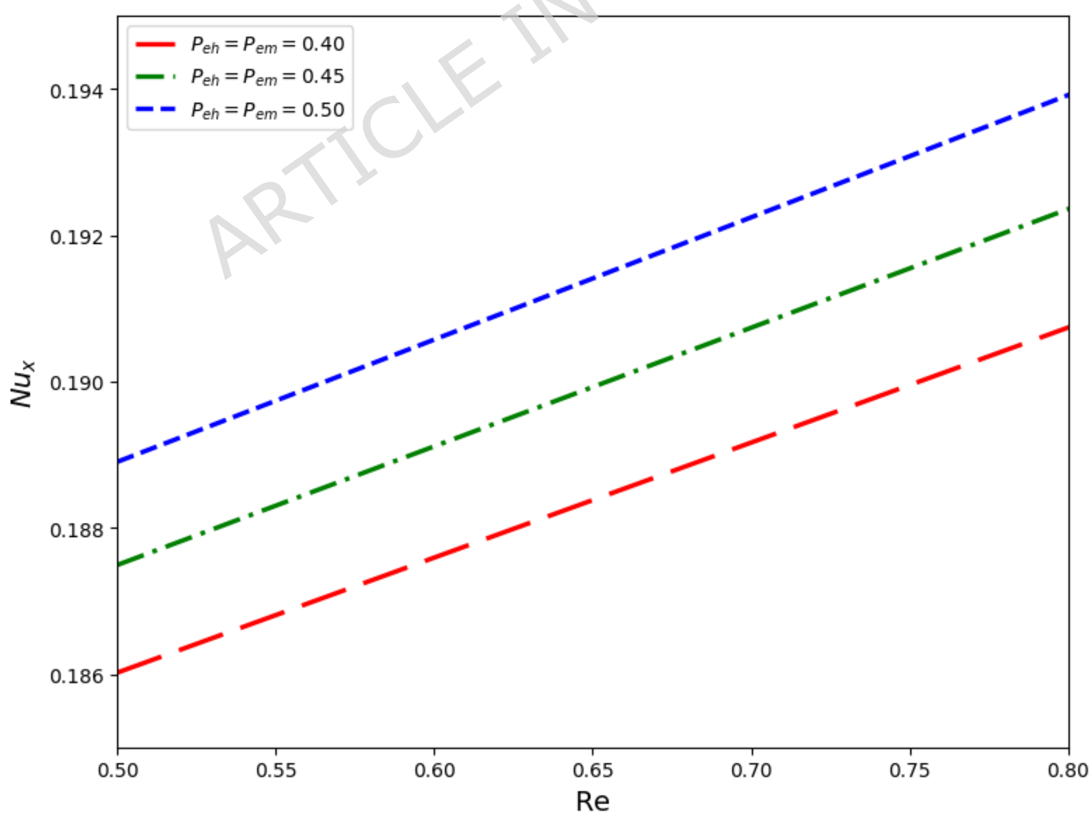


Figure 39: Effect of Reynolds number and Peclet number on Nusselt number at $N_1 = N_2 = N_3 = Z = 1$, $M = 0.5$, $d = 0.5$, $R_d = 0.4$, $E_c = 0.2$, $S_c = S_r = 0.2$, $D_u = 0.4$, $P_r = 1$.

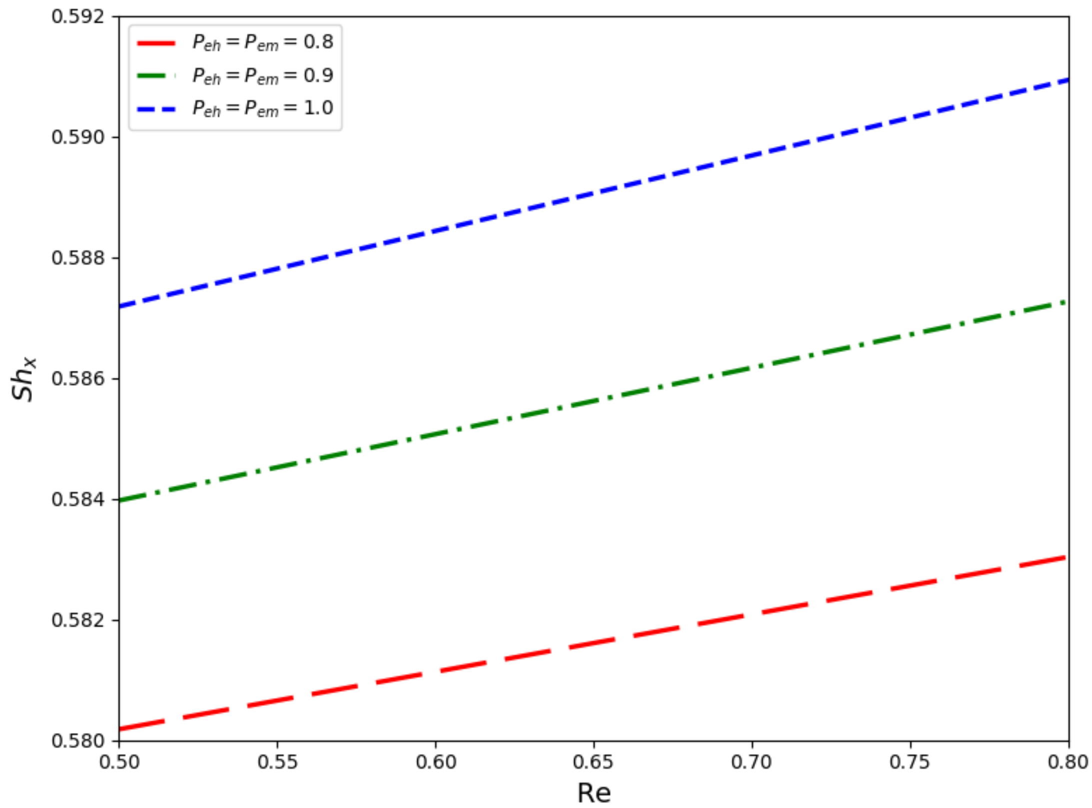


Figure 40: Effect of Reynolds number and Peclet number on Sherwood number.at $N_1 = N_2 = N_3 = Z = 1$, $M = 0.5$, $d = 0.5$, $R_d = 0.4$, $E_c = 0.2$, $S_c = S_r = 0.2$, $D_u = 0.4$, $P_r = 1$.



**References:**


1. Eringen, A. C. Theory of micropolar fluids. *J. Math. Mech.* **16**, 1–18 (1966).
2. Bhargava, R. & Takhar, H. S. Numerical study of heat transfer characteristics of the micropolar boundary layer near a stagnation point on a moving wall. *Int. J. Eng. Sci.* **38**, 383–394 (2000).
3. Anika, N. N., Hoque Md, M., Hossain, S. & Alam Md, M. Thermal diffusion effect on unsteady viscous MHD micropolar fluid flow through an infinite plate with hall and ion-slip current. *Proc. Eng.* **105**, 160–166 (2015).
4. Bhargava, R., Sharma, S., Takhar, H. S., Bég, O. A. & Bhargava, P. Numerical solutions for micropolar transport phenomena over a nonlinear stretching sheet. *Nonlinear Anal. Model. Control.* **12**(1), 45–46 (2007).
5. Takhar, H. S., Agarwal, R. S., Bhargava, R. & Jain, S. Mixed convection flow of a micropolar fluid over a stretching sheet. *Heat Mass Transf.* **34**, 213–219 (1998).
6. Bhargava, R. & Rana, P. Finite element solution to mixed convection in MHD flow of micropolar fluid along a moving vertical cylinder with variable conductivity. *Int. J. Appl. Math Mech.* **7**(1), 29–51 (2011).
7. A. Dawar, et al., Joule heating in magnetohydrodynamic micropolar boundary layer flow past a stretching sheet with chemical reaction and microstructural slip, Case Stud. Therm. Eng. 25 (2021), 100870.

**8.** K.S. Nisar, et al., Cumulative impact of micropolar fluid and porosity on MHD channel flow: a numerical study, Coatings 12 (1) (2022) 93.

**9.** W. Deebani, et al., Convective micropolar fluid over inclined surface with thermal radiation and velocity slip condition effects: duality and stability, Int. J. Mod Phys B 2450114 (2023).

**10.** Ajithkumar M, Sucharitha G, Lakshminarayana P. Cattaneo-Christov heat flow analysis of hydromagnetic micropolar nanofluid over a chemically activated permeable stretching sheet. Indian Journal of Chemical Technology (IJCT). 2025 Sep 27;32(5):593-604.

**11.** Ajithkumar M. Thermo□Solutal Dynamics of Electroactive Casson Nanofluid Flow through an Uneven Asymmetric Conduit for Advanced Microfluidic Applications. Advanced Theory and Simulations. 2025 Dec;8(12):e01148.

**12.** Ajithkumar M, Makinde OD. Thermofluidic Simulation of Magneto-Radiative Viscoelastic Nanomaterial Flow in a Chemically Activated Porous Duct with Double-Diffusive Convection. Results in Engineering. 2025 Dec 4:108594.

**13.** Ajithkumar M, Lakshminarayana P. A study on bioconvective peristaltic flow of a Casson nanofluid in a porous uniform/non□uniform flexible conduit. ZAMM□Journal of Applied Mathematics and Mechanics/Zeitschrift für Angewandte Mathematik und Mechanik. 2024 Dec;104(12):e202300007.

**14.** Maddina DK, Shah NA. Unveiling the thermally dissipative peristaltic pumping characteristics of hydromagnetic nanofluid in an oblique micro-wavy conduit via artificial neural network-based optimization. International Journal of Numerical Methods for Heat & Fluid Flow. 2026 Jan:1-28.

**15.** Hafed ZS, Hussein SA, Alenazi A, Arafa AA, Ahmed SE. Impacts of Arrhenius energy and viscous dissipation on variable properties of viscoelastic nanofluid flow with slip velocity. International Journal of Modelling and Simulation. 2025 Jul 4;45(4):1230-48.

**16.** Alrige, M., Shah, S. S., Haq, R. U., & Algehyne, E. A. (2024). An efficient FEM approach for Soret and Dufour effect in non-Newtonian fluid enclosed between two equilateral triangular cavity. International Communications in Heat and Mass Transfer, 152, Article 107227.

**17.** Ketchate, C. G. N., Kapen, P. T., Fokwa, D., & Tchuen, G. (2024). Instability of MHD mixed convection flow of nanofluid in porous channel with thermal radiation, chemical reaction, Dufour and Soret effects. Chinese Journal of Physics, 87, 728–750.

**18.** Hussain, S., Jamal, M., & Geridonmez, B. P. (2021). Impact of power law fluid and magnetic field on double diffusive mixed convection in staggered porous cavity considering Dufour and Soret effects. International Communications in Heat and Mass Transfer, 121, Article 105075.

**19.** Salahuddin, T., Javed, A., Khan, M., Awais, M., & Bangali, H. (2022). The impact of Soret and Dufour on permeable flow analysis of Carreau fluid near thermally radiated cylinder. International Communications in Heat and Mass Transfer, 138, Article 106378.

**20.** Mohammadi, M., & Nassab, S. G. (2022). Double-diffusive convection flow with Soret and Dufour effects in an irregular geometry in the presence of thermal radiation. International Communications in Heat and Mass Transfer, 134, Article 106026.

**21.** Awais, M., Salahuddin, T., & Muhammad, S. (2024). Effects of viscous dissipation and activation energy for the MHD Eyring-powell fluid flow with Darcy-Forchheimer and variable fluid properties. Ain Shams Engineering Journal, 15(2), Article 102422.

**22.** Seid, E., Haile, E., & Walelign, T. (2022). Multiple slip, Soret and Dufour effects in fluid flow near a vertical stretching sheet in the presence of magnetic nanoparticles. International Journal of Thermofluids, 13, Article 100136.

**23.** Li, S., Imtiaz, M., Khan, M. I., Kumar, R. N., & Akramova, K. S. (2024). Applications of Soret and Dufour effects for Maxwell nanomaterial by convectively heated surface. Numerical Heat Transfer, Part A: Applications, 1–15.

**24.** Mostafa A.A. Mahmoud, Thermal radiation effects on MHD flow of a micropolar fluid over a stretching surface with variable thermal conductivity, Physica A 375 (2) (2007) 401–410.

**25.** Emad M. Abo-Eldahab, Ahmed F. Ghonaim, Convective heat transfer in an electrically conducting micropolar fluid at a stretching surface with uniform free stream, Appl. Math. Comput. 137 (2-3) (2003) 323–336.

**26.** Ahmed SE, Arafa AA, Hussein SA. Viscous dissipation and Joule heating in case of variable electrical conductivity Carreau–Yasuda nanofluid flow in a complex wavy asymmetric channel through porous media. Modern Physics Letters B. 2024 Dec 30;38(36):2450369.

**27.** Nath, Jintu Mani, Tusar Kanti Das, Ashish Paul, and Ali J. Chamkha. "Numerical computation of tangent hyperbolic magnetohydrodynamic Darcy–Forchheimer Williamson hybrid nanofluid flow configuring variable thermal conductivity." Hybrid Advances 7 (2024): 100343.

**28.** Reddy, M. Vinodkumar, Tusar Kanti Das, K. Malleswari, Jintu Mani Nath, S. Saroja, and V. Madhusudana Reddy. "MHD radiative Williamson nanofluid through Darcy Forchheimer medium due to stretching sheet in the presence of heat source, activation energy and motile microorganisms." Indian Journal of Chemical Technology (IJCT) 32, no. 2 (2025): 176-189.

**29.** Das, Tusar Kanti, Ashish Paul, Jintu Mani Nath, and Neelav Sarma. "The Yamada-Ota model-based Casson quadra hybrid nanofluid stagnation flow configured by ohmic heating, heat source, and Newtonian boundary heating across an exponentially stretched cylinder." Partial Differential Equations in Applied Mathematics 14 (2025): 101159.

**30.** F. Mabood, S.M. Ibrahim, M.M. Rashidi, M.S. Shadloo, Giulio Lorenzini, Nonuniform heat source/sink and Soret effects on MHD non-Darcian convective flow past a stretching sheet in a micropolar fluid with radiation, Int. J. Heat Mass Transf. 93 (2016) 674–682.

**31.** M. Ramzan, M. Farooq, T. Hayat, Jae Dong Chung, Radiative and Joule heating effects in the MHD flow of a micropolar fluid with partial slip and convective boundary condition, J. Mol. Liq. 221 (2016) 394–400.

**32.** Naduvinamani NB, Shridevi S (2018) Squeeze film lubrication between porous parallel plates with magneto-hydrodynamic-micropolar fluid. J Nanofluids 7(6):1233–1239.

**33.** Halambi B, Hanumagowda BN (2018) Effects of surface roughness with MHD on the micropolar fluid flow between rough elliptic plates. Int J Mech Eng Technol 9(11):586–598.

**34.** Hayat T, Nawaz M, Hendi AA, Asghar S (2011) MHD squeezing flow of a micropolar fluid between parallel disks. J Fluids Eng. https://doi.org/10.1115/1.4005197

**35.** Bhattacharjee B, Chakraborti P, Choudhuri K (2020) Theoretical investigation of porous hydrostatic journal bearing under micropolar fluid lubrication. Proc Inst Mech Eng Part N J Nanomater Nanoeng Nanosyst 234(1–2):11–18.

**36.** Ouyang, Y., Basir, M.F.M., Naganthran, K. and Pop, I., 2025. Exploring heat generation and magnetic effects on unsteady ternary nanofluid flow over a dynamic wedge in porous media. *Chinese Journal of Physics*, *93*, pp.531-548.

**37.** Ouyang, Y., Md Basir, M.F., Naganthran, K. and Pop, I., 2025. Stability analysis of unsteady ternary nanofluid flow past a stretching/shrinking wedge. *Open Physics*, *23*(1), p.20250148.

**38.** Ascher, U.M., Mattheij, R.M. and Russell, R.D., 1995. Numerical solution of boundary value problems for ordinary differential equations. Society for Industrial and Applied Mathematics.

**39.** Ortega, J.M. and Rheinboldt, W.C., 2000. Iterative solution of nonlinear equations in several variables. Society for Industrial and Applied Mathematics.

**40.** Singh, J., 2022. Shooting method for solving two-point boundary value problems in ODEs numerically. arXiv preprint arXiv:2208.13221.

**41.** Husin, N.Z. and Ahmad, M.Z., 2024. Hybridization of the shooting and Runge-Kutta Cash-Karp methods for solving Fuzzy Boundary Value Problems. AIMS Mathematics, 9(11), pp.31806-31847.

**42.** Butcher, J.C., 2008. Numerical Methods for Ordinary Differential Equations. 2nd ed. Chichester: Wiley.

**43.** N.A. Abdul Latiff, M.J. Uddin, O.A. Beg, A.I. Ismail, Unsteady forced bioconvection slip flow of a micropolar nanofluid from a stretching/shrinking sheet, Proc. Inst. Mech.

Eng. Part N J. Nanoeng. Nanosyst. (2015), http://dx.doi.org/10.1177/1740349915613817.

**44.** P. Sibanda, F. Awad, Fluid Mech. Heat Mass Transfer (2010) 112–120.

**45.** M. Fakour, A. Vahabzadeh, D. Ganji, M. Hatami, Analytical study of micropolar fluid flow and heat transfer in a channel with permeable walls, Journal of Molecular Liquids 204 (2015) 198-204.

**46.** M. Sheikholeslami, M. Hatami, D. Ganji, Micropolar fluid flow and heat transfer in a permeable channel using analytical method, Journal of Molecular Liquids 194 (2014) 30-36.

**47.** Liao, S.J., 2012. Homotopy Analysis Method in Nonlinear Differential Equations. Heidelberg: Springer.

**48.** Jalili, B., Azar, A.A., Jalili, P. and Ganji, D.D., 2023. Analytical approach for micropolar fluid flow in a channel with porous walls. Alexandria Engineering Journal, 79, pp.196-226.

**49.** Mirzaaghaian, A. and Ganji, D.D., 2016. Application of differential transformation method in micropolar fluid flow and heat transfer through permeable walls. Alexandria Engineering Journal, *55*(3), pp.2183-2191.